An Investigation on Secondary Organic Aerosol Induced Restructuring in Soot Aggregates

by

Kaiser K Leung

A thesis submitted in partial fulfillment of the requirements for the degree of

Master of Science

Department of Mechanical Engineering
University of Alberta

Abstract

Currently the understanding of morphological evolution of soot aggregates under the influence of secondary organic aerosol (SOA) and the process of SOA restructuring are not well known. As a consequence, the uncertainty in the estimation of the radiative forcing from soot aggregates is high. The objective of this work is to investigate the relationship between soot restructuring due to SOA coatings and the aggregate properties, and to investigate the effects of water on SOA coatings. Two sets of photo-oxidation experiments were conducted to investigate the restructuring of soot aggregates induced by secondary organic aerosol (SOA) coating and its humidity dependence. The first set of photo-oxidation experiments involved soot aggregates generated from three sources, an ethylene premixed burner, an inverted diffusion burner, and a diesel generator. Soot aggregates were treated by denuding then size-selected by a differential mobility analyzer and injected into a smog chamber, and subsequently exposed to SOA using *p*-xylene as a precursor. For a given initial mobility diameter, the diesel aggregates were less dense with smaller primary particles than the aggregates from the two burners. The change in mobility of aggregates between the initial and final structures displayed a linear dependence on the number of primary particles in the aggregate. The linear relationship could allow modelers to predict the evolution of aggregate morphology induced by SOA using a single parameter. The second set of photo-oxidation experiments investigated the relative humidity (RH) dependence on the restructuring of aggregates induced by SOA coatings. Soot aggregates in these experiments were generated from the ethylene premixed burner, classified by mobility diameter and injected into a smog chamber. The aggregates were then exposed to SOA coatings using *p*--xylene as a precursor and subsequently subjected to one of the RHs: < 12, 20, 40, 60, 85%. At RH < 12%, a uniform mobility growth with increasing coating mass was observed, indicating the

coating was too viscous to induce aggregate restructuring. At RH above 20%, restructuring of aggregates were observed in the form of a decrease in mobility diameter with increasing coating mass. Interestingly the degree of restructuring increased with increasing RH, indicating that elevated humidity decreased coating viscosity and increased surface tension. Appreciable water uptake by the SOA coating was observed for RH above 60%, and the hygroscopicity parameter for SOA coating generated from *p*-xylene was determined. The result of the second series of photo-oxidation experiments has significant implications on atmospheric restructuring of soot aggregates induced by SOA coatings. Overall the significance of the work reported here may contribute to the better understanding of the evolution of soot aggregate morphology due under the influence of SOA coatings in the atmosphere, allowing aggregate modelers to predict the compaction of aggregates knowing the aggregate properties.

Preface

Chapter 2 of this thesis has been submitted to *Environmental Science and Technology* as "Relationship between Soot Aggregate Restructuring Due to Surface Coatings and Primary Particles" by Kaiser K. Leung, Elijah G. Schnitzler, Ramin Dastanpour, Steven N. Rogak, Wolfang Jäger, and Jason S. Olfert. I was responsible for data collection, processing, and analysis as well as manuscript composition. Elijah G. Schnitzler was involved with experimental set up, assisted with data collection and manuscript composition. Ramin Dastanpour assisted in data collection and advised in data processing. Steven N. Rogak assisted in data collection and advised in data analysis. Wolfang Jäger was involved with providing experimental equipment and contributed to manuscript edits. Jason S. Olfert was the supervisory author, involved with the concept formation, data analysis, and manuscript edits.

Chapeter 3 of this thesis has been submitted to *Environmental Science and Technology Letters* as "Relative Humidity Dependence of Soot Aggregate Restructuring Induced by Secondary Organic Aerosol: Effects of Water on Coating Viscosity and Surface Tension" by Kaiser K. Leung, Elijah G. Schnitzler, Wolfang Jäger, and Jason S. Olfert. I was responsible for data collection, processing, and analysis as well as manuscript composition. Elijah G. Schnitzler was involved with concept formation, experimental set up, and manuscript composition. Wolfang Jäger contributed to manuscript edits. Jason S. Olfert was the supervisory author, involved with manuscript edits.

Acknowledgements

I would like to thank Dr. Olfert for his guidance, patience, and support over the course of my studies. He has been extremely helpful and encouraging while always having a relaxed and positive attitude, giving me the confidence to move forward along this journey. I couldn't ask for more in a supervisor.

I would also like to thank Elijah Schnitzler for his guidance, patience and support over the course of my studies. Thank you for the company on those long experiment days, talking about hockey, chemistry, and almost anything. I am grateful for your guidance and input along the way. Also, thank you to everyone else in the research group who have kept me positive or contributed over these years.

Finally, thank you to all my friends and family for keeping me grounded. I want to extend extra recognition to my parents and girlfriend for their love and support. They were with me for each step, pushing me along or I wouldn't have made it to where I am. I am eternally grateful.

Table of Contents

List of Tables

List of Figures

Chapter 1

Introduction and Background

Currently it is accepted that soot aggregates have a negative impact on human health and the environment. For the work presented here, the focus will be the negative impact that soot aggregates have on the environment. Soot aggregates are a major contributor to air pollution and global warming. Soot aggregates in the atmosphere contribute to global warming due to their high absorption of all visible wavelengths of light. The contribution that soot aggregates have on the climate forcing is significant, only second to carbon dioxide (Ramanathan and Carmichael 2008). Soot aggregates are particles composed of carbon primary particles and are emitted into the atmosphere from a wide assortment of sources, classified as either natural or anthropogenic, where classification of the source is dependent on the involvement of human activity. Natural sources of soot aggregates are from biomass burning (Schwarz et al. 2008), and anthropogenic sources would include fossil fuel burning (Penner 1999). The properties of the soot aggregates generally depend on the source and local conditions of combustion.

Recently the properties of soot aggregates have been related to their constituent monomers or primary particles, such that the surface area and mass of aggregates increases with the dispersity in primary particle size (Dastanpour and Rogak 2016). The primary particles are composed of elemental carbon with a characteristic diameter as a result of incomplete combustion at the flame. For a brief time after the formation of the primary particles, collisions occur between the particles via Brownian motion, and the particles begin to adhere. The adhesion between multiple primary particles continues to grow the soot aggregate, and after a certain distance from the flame the aggregate is released into the ambient air (Kholghy et al. 2013). Due to the nature in the formation of soot aggregates, the particles tend to have branched or fractal-

like structures over a finite range of the particle (Sorensen 2011). Generally, the primary particles that constitute a soot aggregate are approximated as identical diameter spheres with point contacts to simplify aggregate structural analysis. However this approximation is not necessarily always the case as the primary particles are sensitive to the local conditions of combustion; where a single soot generating source can produce primary particle diameters ranging between 5 to 55 nm (Barone et al. 2012), a transmission electron microscopy image is provided in Figure 1.1 to demonstrate the dispersity in primary particles.

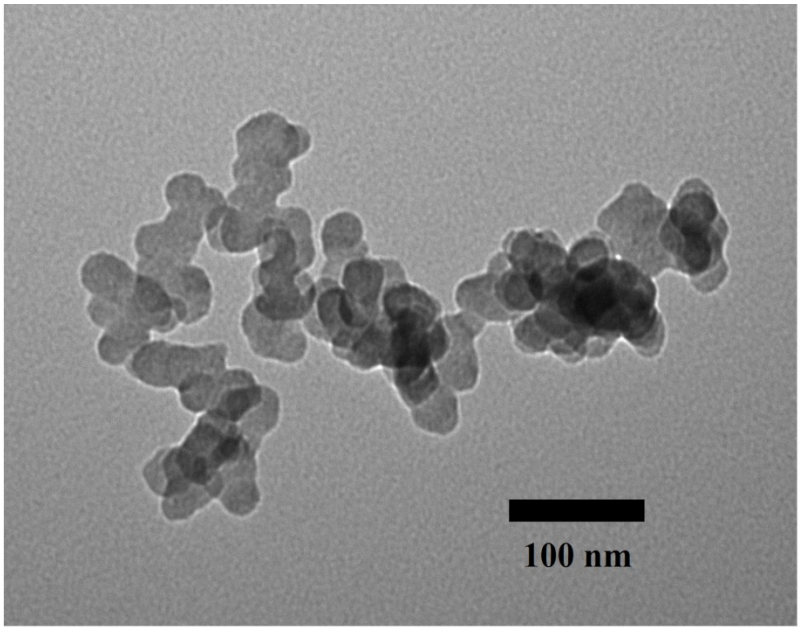

Figure 1.1. Transmission electron microscopy image of a soot aggregate

Due to the negative effects of soot aggregates governments have intervened to reduce the impact of soot aggregate by regulating particle emissions. Global climate models is used to understand the effects of black carbon or soot on climate; however, the uncertainty in the radiative forcing of soot in most climate models are significant, where predictions of radiative forcing ranges between 0.2 to 0.9 W m^{-2} (Bond et al. 2013). The motivation for this study is to reduce the uncertainty in climate models by providing a better understanding on how soot morphology can change with the interaction of gas-phase species in the atmosphere. In this

chapter, a brief introduction to the impact soot aggregates have on climate, an introduction to secondary organic aerosols (SOA), and an overview of this report is given.

1.1 **Climate Impact**

Climate modeling is a great topic of research focus because of interest in climate projections. The climate projections predicted by models vary and one of the biggest uncertainties is the variation in the contributions of aerosols, more specifically the contribution of soot aggregates to global climate change. Soot aggregates are an important species of aerosol because it can affect the climate both directly by absorbing and scattering visible wavelengths of light, and indirectly, through altering cloud albedo (reflectively) (Bond et al. 2013).

One parameter that is commonly used to measure the contribution to global climate change is radiative forcing. Radiative forcing is the difference between the energy flux in and out of the atmosphere, where a positive radiative forcing reduces the rate at which energy leaves the atmosphere and vice versa (Bond et al. 2013). The determination of radiative forcing due to soot aggregates is commonly calculated as the product of four variables which are emissions, lifetime, mass absorption cross section and radiative forcing per unit absorption depth. In this report the variable of interest is the mass absorption cross section, more specifically the radiative forcing is a function of the mass specific extinction cross section (MEC) of the aggregate (Schulz et al. 2006). MEC for a particle is given as the summation of the particle's mass specific absorption cross section (MAC) and mass specific scattering cross section (MSC). The definition of a mass specific absorption cross section is (Radney et al. 2014),

$$\mathrm{MAC} = \frac{\alpha_{\mathrm{abs}}}{m_{\mathrm{p}} N} = \frac{\mathrm{C}_{\mathrm{abs}}}{m_{\mathrm{p}}} \tag{1.1}$$

Where N is the number density of particles, m_{p} is the average mass of particles, α_{abs} is the absorption coefficient, and $\mathrm{C}_{\mathrm{abs}}$ is the particle absorption cross section in m^2. The absorption

coefficient is the fractional loss in light intensity per-unit-propagation distance in m^{-1}, and is also the product of N and C_{abs},

$$\alpha_{abs} = NC_{abs} \tag{1.2}$$

The absorption coefficient is also related to the refractive index of soot aggregates and the wavelength of light, and can be determined with the following relationship (Bohren 1983),

$$\alpha_{abs} = \frac{4\pi k}{\lambda} \tag{1.3}$$

Here, k is the imaginary component of the refractive index, and λ is the wavelength of light. The refractive index, m, is defined as $m = m' - m'ki$, where m' is the real component of refractive index (Hinds 1999). This definition for the MAC is similar to the definition of MSC and MEC, where the terms α_{abs} and C_{abs} are interchanged for their counterparts (α_{sca},C_{sca} and α_{ext},C_{ext} for scattering and extinction, respectively). Coatings can form on soot aggregates in the atmosphere with the interaction with other gas-phase species altering the optical properties, MEC in particular, of the soot aggregates through restructuring and lensing (Khalizov et al. 2009; Radney et al. 2014). Restructuring of an aggregate is the process in which the organization of the primary particles within the aggregate are changed, usually into a more compact form due to external forces. Lensing refers to the property where the coating formed on aggregates can act as a lens, focusing a larger area of light onto the absorbing soot aggregate. Since the optical properties of an aggregate can change through structure and lensing effects, this report will focus on the structure aspect of soot. A significant species that interact with soot aggregates are known as SOA.

Atmospheric aerosols that are emitted directly from their sources are considered to be primary aerosols; however there is a class of aerosols known as secondary aerosols which are formed in the atmosphere. In a study by Goldstein and Galbally (2007), using a top-down

estimate of the global aerosol budget, 76% of aerosols are estimated to be secondary aerosols. A class of secondary aerosol that will be the focus of this report is SOA. SOA are formed from the gas-phase oxidation of biogenic and anthropogenic volatile organic compounds (VOC) (Mentel et al. 2009; Shao et al. 2016).

VOC is a chemical class emitted into the atmosphere with generally high vapour pressures due to their chemical composition, and can be classified as either biogenic or anthropogenic. Biogenic VOC species, such as isoprene, terpenes, alkanes, alkenes, alcohols, and many more, are emitted from vegetation (Kesselmeier and Staudt 1999); and anthropogenic VOC species, toluene, *p*-xylene, *m*-xylene for example, are generated from burning of fossil fuels (Piccot et al. 1992). VOC in the atmosphere can undergo further processing via oxidation reactions that occur from the interactions with atmospheric hydroxyl radicals, ozone, or photolysis (Hallquist et al. 2009). The oxidation reaction results in species containing many combinations of oxygenated functional groups, including aldehyde, ketone, alcohol, nitrate, and carboxylic acid group. The resulting oxidation products can therefore lead to many thousands of combinations of mixtures with varying properties (Goldstein and Galbally 2007). However, if one specific precursor is oxidized then the resulting mixture will lead to a combination of products due to the "branching ratios", which is the likelihood that a specific product is formed over other possible products.

Formation of SOA is result of the partitioning of the VOC oxidation products. The theory of gas-particle partitioning developed by Pankow (1994) and Odum et al. (1996) involves the balance of the species between the gas and particle phase. The governing equation describing this phenomenon is as follows:

$$K_p = \frac{C^p}{C^g C_{OA}} \tag{1.4}$$

Where C^g ($\mu g\ m^{-3}$) is the mass concentration of the species per unit volume of air in the gas phase, C^p ($\mu g\ m^{-3}$) is the mass concentration of the species per unit volume of air in the particle phase, K_p ($m^3\ \mu g^{-1}$) is the equilibrium partitioning coefficient, and C_{OA}($\mu g\ m^{-3}$) is the mass concentration of the suspended particles per unit volume of air. In the photo-oxidation experiments performed in later chapters, the continual growth of the particles or the increase in coating mass is driven by the continual increase in C^g of the oxidation products assuming K_p and C_{OA} remain constant.

The structure that soot aggregates have upon emission is not permanent and can be changed with the interaction between other internally-mixed non-absorbing species in the atmosphere. More specifically, compaction of soot aggregates can occur when sufficient coating mass of an external species such as water (Pagels et al. 2009; Ma et al. 2013; Mikhailov and Vlasenko 2007), oleic acid (Ghazi and Olfert 2013; Bambha et al. 2013), sulfuric acid (Khalizov et al. 2009), and SOA (Qiu et al. 2012; Schnitzler et al. 2014). This compaction is the result of attractive forces acting on the primary particles created by the coating through liquid bridging or capillary forces. Liquid bridging is the result of liquid forming between two rigid bodies; a force is exerted onto the two rigid bodies by the liquid in an attempt to reduce the surface energy. The force exerted onto the two surfaces by liquid bridging is described in detail by Lian et al. (1993). From their results it was found that the forces scale with the diameter of primary particles and the surface tension of the liquid. Similarly, the capillary force acting on the primary particles is the result of the liquid reducing the energy in the interface between the coating and particle; the capillary forces are also driven by the surface tension of the coating (Kralchevsky et al. 1995; Kralchevsky and Nagayama 2000). Therefore, an important property influencing the extent of aggregate restructuring is the surface tension of the induced coating. The dependence of

restructuring on the coating surface tension is further emphasized in a recent study by Schnitzler et al. (2017) where initially fractal soot aggregates generated from a McKenna burner were coated with materials of different surface tensions. The results showed that coatings of glycerol (surface tension of 64 $\mathrm{mN\,m^{-1}}$ at 20 °C) induced more aggregate compaction than coatings with a lower surface tension, tridecane for example (surface tension of 26 $\mathrm{mN\,m^{-1}}$ at 20 °C) (Schnitzler et al. 2017).

Since the MEC of an aggregate is composed of both MSC and MAC, recent studies have investigated the evolution of both MAC and MSC of soot with respect to the coating or structure of the aggregate. In a study conducted by Radney et al. (2014), the MSC of an aggregate was found to increase with a compact particle. Currently, it is undetermined if the morphology of the soot aggregates affect the MAC. One study by Liu et al. (2008) found that the MAC for a compact aggregate was higher than their fractal counterpart, but on the contrary, a study by Kahnert and Devasthale (2011) reported a lower MAC for compact aggregates.

1.2 **Measurement Instruments**

In the following work, the soot properties were determined using three instruments: a differential mobility analyzer (DMA), a centrifugal particle mass analyzer (CPMA), and a condensation particle counter (CPC). The DMA is used to classify particles with respect to the mobility diameter, and the CPMA is used to classify particles with respect to mass. The CPC is used to determine the number of particles at the sample inlet.

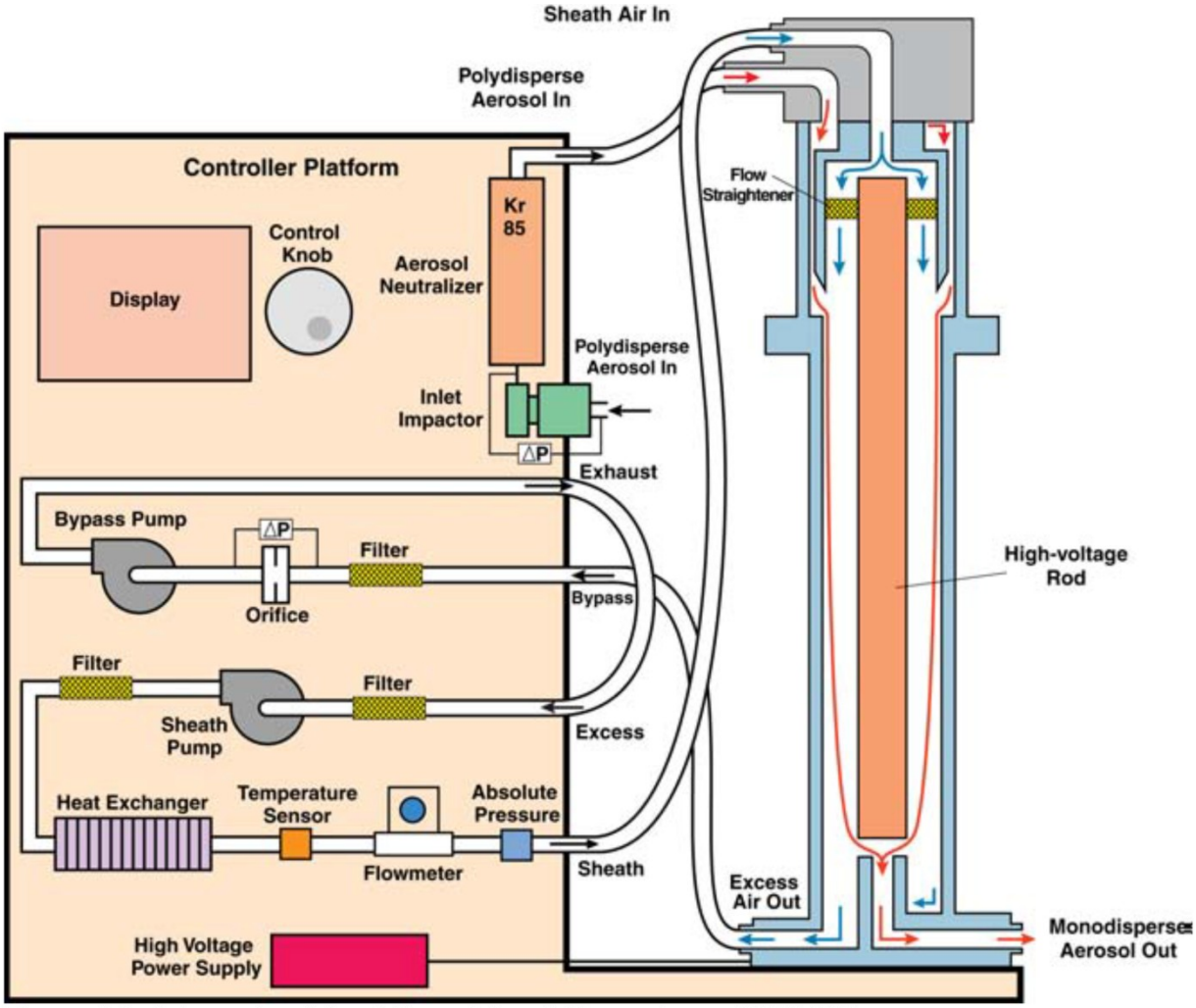

Figure 1.2. Schematic of the differential mobility analyzer (TSI 2009)

The DMA is an instrument that classifies sample particles by the electrical mobility diameter. It selects the electrical mobility diameter of particles using the balance between electrostatic forces on a charged particle to the drag force experienced by the particle. The equation for electrical mobility is as follows (TSI 2009),

$$Z_p = \frac{neC}{3\pi\mu D_p} \tag{1.5}$$

Where n is the elementary charges on the particle, e is the elementary charge, C is the Cunningham slip correction, μ is the gas viscosity, and D_p. A schematic of the DMA internal structures are depicted in Figure 1.2 (TSI 2009). The aerosol sample that enters the DMA is first

directed into a neutralizer so that the particles in the sample will carry a known charge distribution, and the particles are then directed into the main column of the DMA. The main column of the DMA consists of two concentric metal cylinders, where the sample flow and a sheath flow is introduced at the top of the column. The central cylinder is controlled to a set negative voltage (see in Figure 1.2) which attracts the charged particles towards the center. However due to the geometry and voltage of the column, only particles that fall into a narrow band of electrical mobility diameters can leave the column via the aerosol outlet.

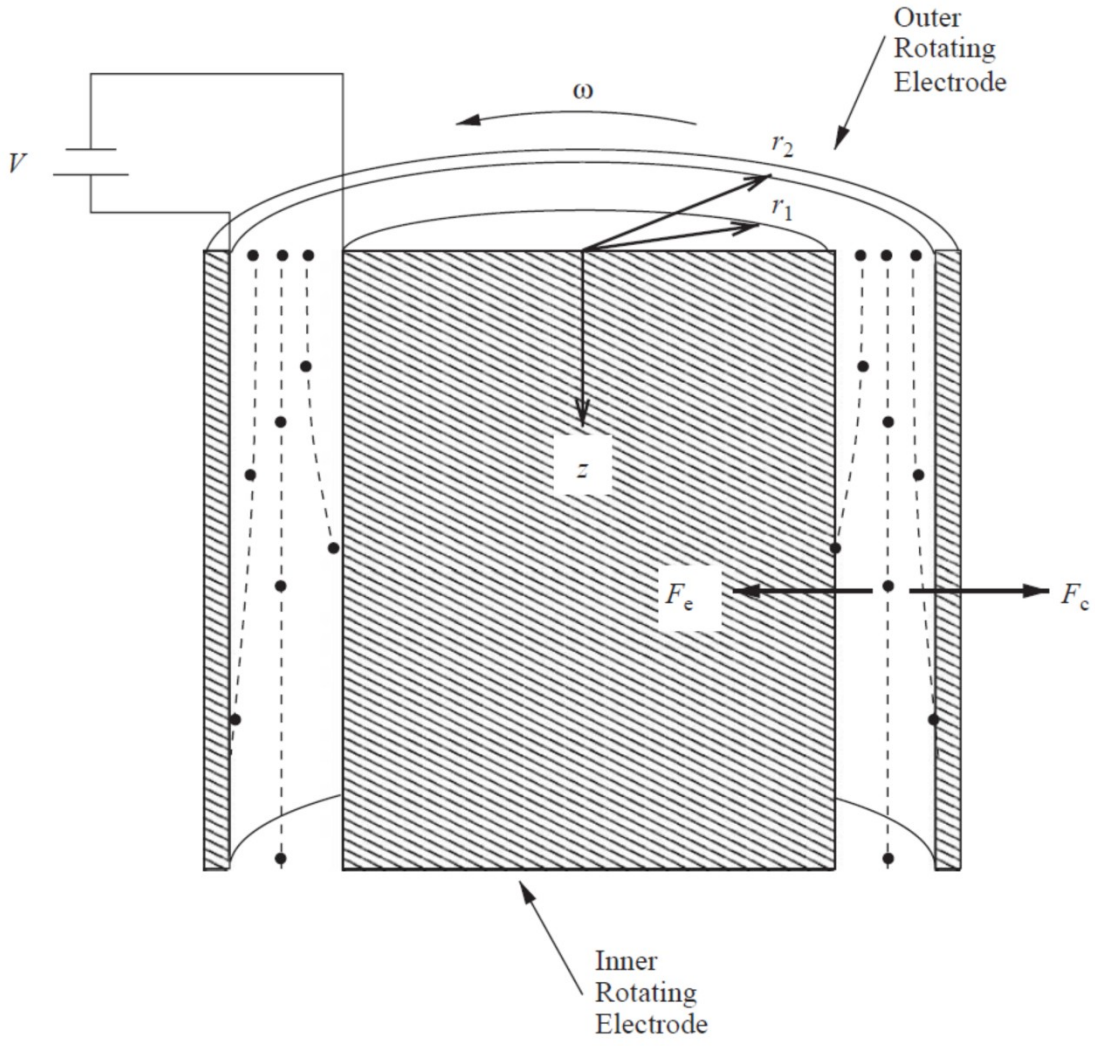

Figure 1.3. A cross section of the particle mass analyzer (Olfert and Collings 2005)

The CPMA is an instrument that classifies particles by the mass to charge ratio of the particle by balancing the centrifugal and electrostatic forces using two concentric cylinders and a voltage. A cross section of the cylinder is depicted in Figure 1.3. The charged aerosol sample is directed into the space between the two concentric cylinders, which then flows along the cylinder. The concentric cylinders rotate at their set angular velocity and the result is a centrifugal force that acts on the particles in the sample flow, directed to the outside cylinder. In addition to the rotation, a voltage is applied across the concentric cylinders and the electrostatic force draws the charged particles towards the inner cylinder. Knowing the rotational speed and voltage applied to the cylinders, only particles that fall within a narrow range of mass to charge ratio can leave the cylinder without being deposited along the cylinder.

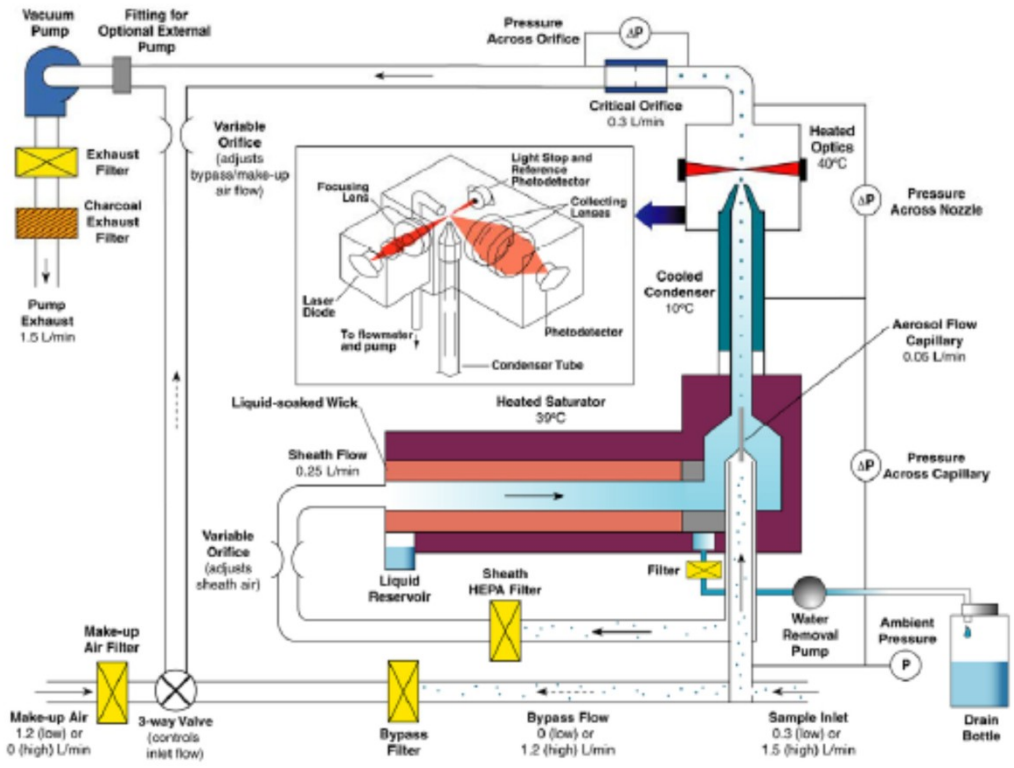

Figure 1.4. Schematic of the condensation particle counter (TSI 2006)

The CPC is an instrument that counts the particles per unit volume in the sample flow and can be paired with a DMA or CPMA to determine the mobility diameter or mass distribution of a sample, respectively. A schematic of the internal components of the CPC is shown in Figure 1.4. The inlet flow into the CPC is split into sample and bypass flows, such that the sample flow is only 0.3 lpm. The sample flow is again split into a smaller sample flow and a sheath flow. The sheath flow passes through a filter to remove any particles and then directed into the saturator. The sheath flow is then saturated with the condensing vapor (butanol in this case). The saturated sheath flow and the sample flow are then rejoined into a condenser which allows the saturated vapor to condense onto the particles in the sample flow, growing the particles. The enlarged particles are then counted by a laser and photodetector to give a particle count per unit volume.

1.3 **Overview**

In this research, soot aggregate restructuring induced by surface coatings of SOA were investigated through series of photo-oxidation experiments. The goal of this work is two-fold: the first is to provide a better understanding of the interaction between SOA coatings and soot aggregate morphology, the second is to investigate the role of water in SOA coatings during the process of aggregate restructuring. The result may lead to the base for a future model for predicting the extent of soot aggregate restructuring with respect to soot properties, thereby increasing the accuracy of future simulations of soot aggregates in the atmosphere. A CPMA, DMA, and CPC were used to characterize the soot with regards to mass-mobility exponents, effective densities and dynamic shape factor. Chapter 2 investigates the extent of aggregate restructuring induced by SOA coatings from three separate soot generating sources, an ethylene premixed burner, a methane inverted diffusion burner, and a diesel generator, to the primary particles in an aggregate. Chapter 3 investigates the relative humidity dependence of SOA

coatings to the restructuring of soot aggregates. Chapter 4 provides a summary of the work done and presents conclusions, followed by possible future work.

Chapter 2.

Relationship between Soot Aggregate Restructuring Due to Surface Coatings and Primary Particle Number

2.1 **Introduction**

Soot aggregates in the atmosphere have a significant warming effect on Earth's climate, second only to that of carbon dioxide (Ramanathan and Carmichael 2008), due to strong absorption of all visible wavelengths of light by their constituent primary particles of elemental carbon (Bond and Bergstrom 2006). Soot aggregates form at their sources, which include fossil fuel combustion (Olfert et al. 2007; Park et al. 2003) and biomass burning (Keywood et al. 2013; Schwarz et al. 2008), by collisions between primary particles, giving the soot a branched or fractal-like structure (Sorensen 2011). Depending on the source and the combustion conditions, the primary particles may vary from 5 to 60 nm in diameter (Barone et al. 2012; Gysel et al. 2012), and aggregates may comprise tens to hundreds of primary particles (Sorensen 2011).

The structural and optical properties of soot aggregates can be affected by internally-mixed non-absorbing species. For example, restructuring of soot aggregates from initially branched structures to comparably compact structures can be induced by coatings of many species, including water (Pagels et al. 2009; Ma et al. 2013; Mikhailov and Vlasenko 2007), heptane (Mikhailov and Vlasenko 2007), ethanol (Miljevic et al. 2012), dioctyl sebecate (Ghazi and Olfert 2013), oleic acid (Ghazi and Olfert 2013; Bambha et al. 2013), glutaric acid (Xue et al. 2009), and sulfuric acid (Pagels et al. 2009; Khalizov et al. 2009). The evolution of the optical properties of soot aggregates as a result of restructuring and/or lensing has recently been investigated, both experimentally (Radney et al. 2014) and theoretically (Liu et al. 2016). For a

bare soot aggregate of a given mass, a compact structure results in a greater extinction cross section than a branched structure; however, this is due to increased scattering, not absorption, so compaction may not necessarily lead to an increased warming effect on climate (Radney et al. 2014). On the other hand, the presence of a coating on the aggregate may result in increased absorption even for a compact structure due to lensing, and this enhancement may lead to an increased warming effect (Cappa et al. 2012). Thorough knowledge of the morphological evolution of soot induced by coatings is necessary to further our understanding of the complex climate effects of soot.

In the atmosphere, soot aggregates are exposed to many gas-phase species that may condense and contribute to coatings. Accordingly, it is important to investigate the morphological evolution of aggregates upon coating with mixtures, in addition to neat species. Secondary organic aerosol (SOA), which forms from the photo-oxidation of biogenic and anthropogenic volatile organic compounds (Mentel et al. 2009; Shao et al. 2016), is a mixture of numerous oxygenated organic species. Soot aggregate restructuring has been induced by SOA coatings generated from isoprene (Khalizov et al. 2013), α-pinene (Schnaiter 2005; Saathoff et al. 2003), benzene (Schnitzler et al. 2014), toluene (Schnitzler et al. 2014; Qiu et al. 2012), ethylbenzene (Schnitzler et al. 2014), and *m*- and *p*-xylene (Schnitzler et al. 2014; Guo et al. 2016). Very recently, the changes in morphological and optical properties of burner-generated soot aggregates exposed to ambient air in Beijing and Houston were investigated (Peng et al. 2016). Since fossil fuel combustion is a significant source of ambient soot aggregates, it is also important to investigate restructuring of engine-generated aggregates, in addition to aggregates generated by typical laboratory burners. The evolution of soot aggregates produced by a diesel engine upon photo-oxidation of gas emissions has been investigated in the past (Tritscher et al.

2011). More specifically, previous studies have demonstrated how the properties of the coatings affect restructuring; for example, it was found that the extent of restructuring increases with increasing coating mass (Ghazi and Olfert 2013; Schnitzler et al. 2014) and/or surface tension (Schnitzler et al. 2017). However, the question of how the properties of the aggregates themselves, including primary particle size and number, dictate restructuring has not been the focus of any previous studies.

Here, we investigate the effects of the soot aggregate properties by systematically comparing the coating-induced restructuring of engine- and burner-generated aggregates. We describe a series of smog chamber experiments in which SOA coatings derived from *p*-xylene, a representative anthropogenic precursor (Simpson et al. 2010), were used to restructure mono-disperse soot aggregates from three sources: a McKenna premixed burner, an inverted diffusion burner, and a commercial diesel generator. The morphological evolution of both the coated particles and core soot aggregates was characterized in terms of effective densities, dynamic shape factors, and mass-mobility relationships, derived from masses and mobilities measured using a centrifugal particle mass analyzer (CPMA) and differential mobility analyzer (DMA), respectively. The initial and final morphologies of the aggregates were also characterized using transmission electron microscopy (TEM). The primary particle sizes and numbers were determined using an indirect method, based on *in situ* CPMA and DMA measurements, and a direct method, based on *ex situ* transmission electron microscopy (TEM) samples. The dependence of restructuring on aggregate properties is explored in detail, and the atmospheric implications are discussed. Our study provides key insights for modeling the evolution of the morphological and, in turn, optical properties of soot aggregates.

2.2 **Experimental Section**

2.2.1 **Soot generation and treatment.**

Soot was produced using a McKenna premixed burner (Holthuis & Associates), a custom-built inverted diffusion burner, and a commercial diesel generator (Yanmar, YDG3700). The respective experimental setups for the treatment (to remove volatile and semi-volatile species), and injection of soot are shown in Figure 2.1. The treatment setup for the McKenna burner experiments is shown in Figure 2.1a. Ethylene was used as fuel, and the equivalence ratio was set to two, achieved with ethylene and air flow rates of 1.1 and 8.0 L min^{-1}, respectively. Soot was sampled 27 cm above the flame into an ejector dilutor (Air-Vac, AVR038H), set to a dilution ratio of three, using 30 psi of nitrogen. The ejector dilutor was used to sample the soot aggregates and reduce the water vapor in the sample. The soot particles were then treated by passing them through a 25 cm diffusion drier consisting of tubular mesh surrounded by anhydrous calcium sulfate (Hammond Drierite Co.), further reducing the water vapor in the sample. The sample was then directed into a thermo-denuder, which consists of ¼" tubing and is 25 cm length, set to 573 K, and a counter-flow parallel-plate membrane denuder to remove remaining trace gases (Ruiz et al. 2006).

The treatment setup for the inverted burner experiments is shown in Figure 2.1b. The inverted burner is a successor to the one used by Ghazi et al. (2013). Methane was used as fuel, and the equivalence ratio was set to 0.76, achieved with methane and air flow rates of 1.3 and 16.0 L min^{-1}, respectively. In addition to the combustion air, clean filtered air was used for dilution, at a flow rate of approximately 40 L min^{-1}. The soot was sampled downstream of the dilution phase and directed to the treatment train, which is similar to that used for the McKenna premixed burner, with one addition. In control experiments performed with the above treatment, OH exposure (without injection of *p*-xylene) induced restructuring of inverted burner aggregates

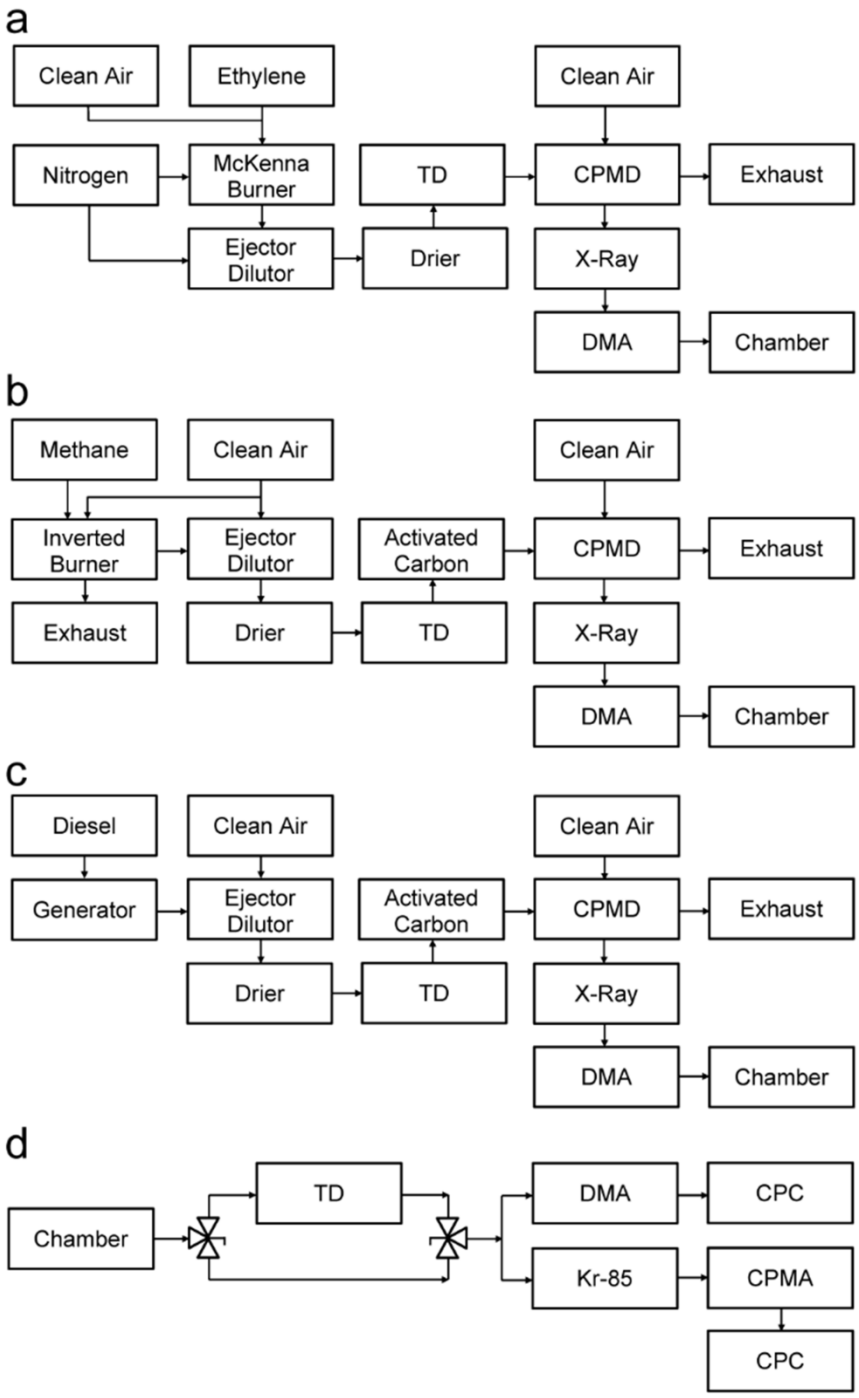

Figure 2.1. Experimental setups during injection of soot aggregates generated by (a) the McKenna premixed burner, (b) the inverted diffusion burner, and (c) the commercial diesel generator and (d) during sampling. TD: thermo-denuder; CPMD: counter-flow parallel-plate membrane denuder; DMA: differential mobility analyzer; CPC: condensation particle counter; CPMA: centrifugal particle mass analyzer.

but had no effect on McKenna burner aggregates. This discrepancy suggests that an appreciable

fraction of trace gas emissions of the inverted burner penetrated the treatment train, and were oxidized in the chamber to form SOA. Since our objective is to compare restructuring of soot from different sources, it is critical that the SOA coatings are derived solely from *p*-xylene, so the background SOA formation is unsatisfactory. Consequently, we introduced a 91-cm tube consisting of tubular mesh surrounded by activated carbon between the thermo- and membrane denuders. In subsequent control experiments, OH exposure alone did not cause restructuring of inverted burner aggregates, so this treatment is sufficient.

The treatment setup for the diesel generator experiments is illustrated in Figure 2.1c. A series of resistors was used to run the engine at set loads. In a set of preliminary experiments, aggregates from the diesel generator were directed to the first DMA, and the size-selected aggregates were then directed alternately with and without thermo-denuding into parallel

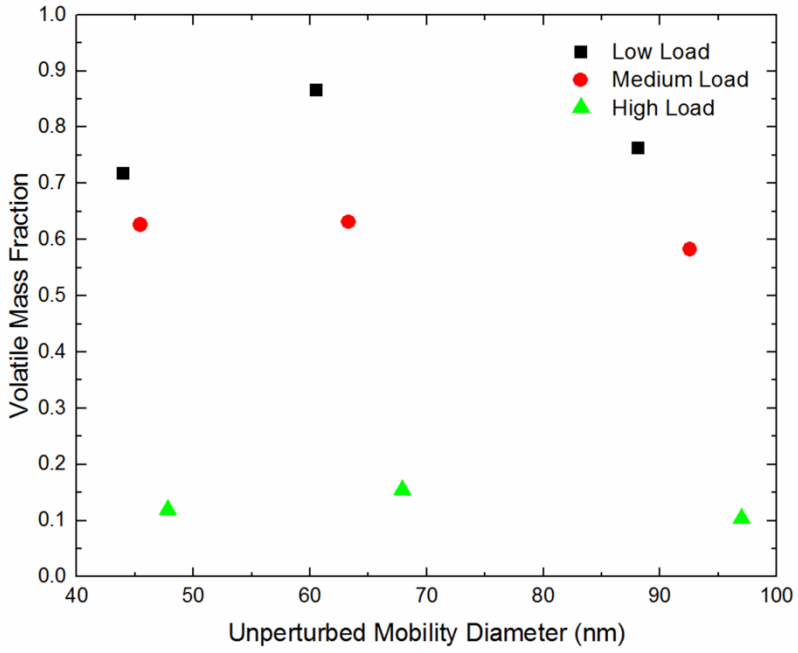

Figure 2.2. Volatile mass fraction of soot aggregates from the diesel generator at various loads.

systems to measure mobility diameter[1] and mass. Volatile mass fraction was calculated as the mass of denuded aggregates over the mass of unperturbed aggregates (Dickau et al. 2016). The purpose in determining volatile mass fraction was to find a load setting on the generator that creates the lowest mass of volatile material mixed into the soot aggregates. As shown in Figure 2.2, an approximately 100% load (3.5 kW) resulted in particles with the lowest volatile mass fraction (13%). Flexible metal tubing was fastened to the exhaust of the engine, and a sample port was drilled 23 cm downstream. The soot particles were then passed through the same treatment train as was used for the inverted burner, including the activated carbon denuder.

After treatment, the soot aggregates were neutralized using an X-ray source (TSI, 3087) and classified by mobility diameter using a DMA (TSI, 3081), which was operated with sample and sheath flow rates of 1.0 and 10.0 L min^{-1}, respectively. The size-selected (70, 100, 150, 200, or 250 nm), mono-disperse aggregates were then injected into the smog chamber, which has been used by Parsons et al. (2011). The 1.8 m^3 cubic chamber is constructed of 0.127 mm thick perfluoroalkoxy film (Ingeniven) and equipped with three sets of eight 32 W black-lights with peak emissions at 350 nm. Perfluoroalkoxy and stainless steel, where appropriate, tubing was used to create inlet and outlet channels for the chamber. Clean air is provided by a pure air generator (Aadco, 737), and the contents of the chamber are circulated by a mixing fan. Ultraviolet differential optical absorption spectroscopy was used to measure concentrations of *p*-xylene by passing broadband emission from a deuterium lamp (Ocean Optics, D-2000-S) through the chamber to a spectrometer (Ocean Optics, HR-2000+).

[1] The mobility diameter of a particle refers to electrical mobility diameter, d_{m}, which is the diameter of a singly charged sphere that has the same ratio of drag to electrostatic forces in a given electric field as the particle

2.2.2 **Precursor photo-oxidation and soot restructuring.**

When soot injection was completed, the soot in the chamber was directed, alternately with and without thermo-denuding, into parallel systems to measure the mean mobility diameter and mass of the particles. A DMA and condensation particle counter (CPC; TSI, 3776) were used to measure the mean mobility diameter, by stepping the DMA through a range of diameters and measuring the particle concentration at each step with by the CPC. The mean particle mass was measured by stepping a CPMA, which classifies particles by their mass-to-charge ratio, through a range of particle masses and measuring the particle concentration with another CPC (TSI, 3771). To improve our particle mass determination, the particles directed to the CPMA were re-neutralized back to a singly-charged state, using a Kr-85 neutralizer (TSI, 3077), to isolate the particle mass peak (Radney and Zangmeister 2016). Soot was monitored continuously for approximately one hour after injection to confirm that there was no background change in mobility diameter or mass. Then *p*-xylene (Fisher, 99.9%) was injected into the chamber to give a concentration of approximately 1 ppm. This concentration, which is too high to be atmospherically representative, is required to probe a wide range of coating masses; also, it has been shown that different initial precursor concentrations lead to the same extent of restructuring at a given coating mass (Qiu et al. 2012), so the effects reported here, particularly at low coating masses, are likely relevant to atmospheric conditions. Precursor concentrations higher than 1 ppm have been used, for example, in studies of the optical properties of SOA (Liu et al. 2013). Hydrogen peroxide (Sigma, 30% w/w in water) was then injected into the chamber to yield hydroxyl radicals by photolysis with UV radiation (Atkinson 2009), which was applied continually throughout the experiment.

Restructuring, or the collapse of the soot particles, is described in terms of mass-mobility exponent, effective density, and shape factor. The mass-mobility exponent, D_{m}, describes how the particle mass, m_{p}, scales with mobility diameter, d_{m}, according to

$$m_{\mathrm{p}} = C d_{\mathrm{m}}^{D_{\mathrm{m}}} \tag{2.1}$$

where C is the mass-mobility prefactor (Park et al. 2003). The mass-mobility exponent is an indication of the structure of the aggregate and ranges between one and three $(1 < D_{\mathrm{m}} < 3)$. Particles with a low D_{m} have a more fractal structure and are more spherical as D_{m} approaches three, where spherical particles have $D_{\mathrm{m}} = 3$. A distinction must be made between the mass-mobility exponent and the fractal dimension because of the usage in literature. The fractal dimension of a particle is a measure of the scaling in the number of primary particles in an aggregate to the aggregate's radius of gyration; the radius of gyration is the inertia of the particle or the distribution of mass about the center of the particle (Sorensen 2011). By definition, the fractal dimension only accounts for the morphology of the particle in a vacuum, whereas the mass-mobility exponent includes the viscosity of the fluid. The effective density, ρ_{eff}, of a particle is the mass of the particle divided by its mobility-equivalent volume[2], $(6m_{\mathrm{p}})/(\pi {d_{\mathrm{m}}}^3)$. In the following discussion, the effective densities of coated and coated-denuded particles are denoted as $\rho_{\mathrm{eff}}^{\mathrm{c}}$ and $\rho_{\mathrm{eff}}^{\mathrm{cd}}$, respectively.

The dynamic shape factor, χ, is a correction parameter to account for the increased drag experienced by an irregular shape particle relative to its spherical equivalent (volume or mass). This parameter is added because irregular shaped particles have a greater surface interaction with the gas/fluid than its volume equivalent spherical counterpart (DeCarlo et al. 2004). By

[2] The mobility-equivalent volume is defined as a sphere with a diameter equal to the mobility, $v_{\mathrm{me}} = (\pi d_{\mathrm{m}}^3)/6$.

definition, the shape factor is the ratio of particle resistance force to the resistance force of a sphere having the same volume and relative velocity, $\chi = F_{D,particle}/F_{D,sphere}$ (Hinds 1999). Using Stokes law for drag, the governing equation for drag is $F_D = 3\pi\mu V d/C_c$, where μ is the viscosity of the gas/liquid, V is the relative velocity of the particle with respect to the fluid, d is the diameter of a sphere. Under Stokes law, the particle of interest flows within the fluid where no-slip conditions exist on the surface of the particle; however due to the size of soot aggregates, this assumption (no-slip) is no longer valid and a correction factor must be introduced. This correction factor is known as the Cunningham slip correction, C_c, and is defined as (Hinds 1999),

$$C_c = 1 + \frac{\lambda}{d}\left[2.34 + 1.05\exp\left(-0.39\frac{d}{\lambda}\right)\right] \tag{2.2}$$

Here λ is the mean free path of the gas. In the case of air at standard ambient temperature and pressure, the mean free path is calculated to be 0.066 μm (Hinds 1999). Including the Cunningham slip correction the equation governing drag becomes $F_D = 3\pi\mu V d_e/C_c(d_e)$. Substituting the equation for drag into the definition of dynamic shape factor, the dynamic shape factor becomes,

$$\chi = [d_{\mathrm{m}} C_{\mathrm{c}}(d_{\mathrm{ve}})]/[d_{\mathrm{ve}} C_{\mathrm{c}}(d_{\mathrm{m}})] \tag{2.3}$$

Where d_{ve} is the volume equivalent diameter, which is the hypothetical diameter of a spherical particle with the same volume. Assuming there are no internal voids (*i.e.* empty regions within the particle that are isolated from the bulk gas phase (DeCarlo et al. 2004)), d_{ve} is

$$d_{\mathrm{ve}} = \left[\frac{6}{\pi}\left(\frac{m^{\mathrm{c}}_{\mathrm{soot}}}{\rho_{\mathrm{soot}}} + \frac{\left(m^{\mathrm{c}}_{\mathrm{p}} - m^{\mathrm{c}}_{\mathrm{soot}}\right)}{\rho_{\mathrm{SOA}}}\right)\right]^{\frac{1}{3}} \tag{2.4}$$

where ρ_{soot} and ρ_{SOA} are the material densities of soot and SOA, respectively, and $m^{\mathrm{c}}_{\mathrm{soot}}$ and $m^{\mathrm{c}}_{\mathrm{p}}$ are the masses of the initial soot aggregates (before the injection of *p*-xylene) and the coated particles (after photo-oxidation), respectively. Again, the superscript denotes that neither type of

particles was thermo-denuded after sampling from the chamber. The difference $m_{\mathrm{p}}^{\mathrm{c}} - m_{\mathrm{soot}}^{\mathrm{c}}$ gives the mass of the SOA coating. The density of soot was taken as 1.8 g cm^{-3} (Park et al. 2004), and the density of the *p*-xylene-derived SOA was taken as 1.46 g cm^{-3} (Nakao et al. 2013). For spherical particles, d_{m} will be equivalent to d_{ve}, and the shape factor will be unity. The shape factors of coated and coated-denuded particles are denoted as χ^{c} and χ^{cd} respectively.

Restructuring was also probed using TEM. To this end, mobility-classified particles were collected on TEM grids using a thermophoretic particle sampler (TPS). Images were produced by a Hitachi H7600 transmission electron microscope operated at 80 kV. Images were analyzed by an open-source automated TEM image processing program, which uses the pair correlation method (PCM) (Dastanpour et al. 2016a; Dastanpour et al. 2016c). This program enables measuring of the average primary particle diameter and various morphology parameters of aggregates.

2.3 **Results and Discussion**

2.3.1 **Initial aggregate morphology**

The initial aggregate morphology is measured to compare it to the morphology from other common sources. The mass-mobility relationships for the initial aggregates are depicted in Figure 2.3a. The dashed curves show linear least-squares fits to the natural logarithms of aggregate mass and mobility; the data points are weighted by their uncertainties, calculated from experimental precision and instrumental bias. The mass-mobility exponents for aggregates from the three sources are all significantly less than three, indicating that their effective densities decrease with increasing mobility diameter. This trend is well-known and has been previously observed for soot generated by laboratory burners (Schnitzler et al. 2014; Ghazi et al. 2013) and diesel engines (Olfert et al. 2007; Park et al. 2003). The mass-mobility exponents of the

aggregates from the McKenna and inverted burners are 2.20 and 2.33, respectively. The mass-

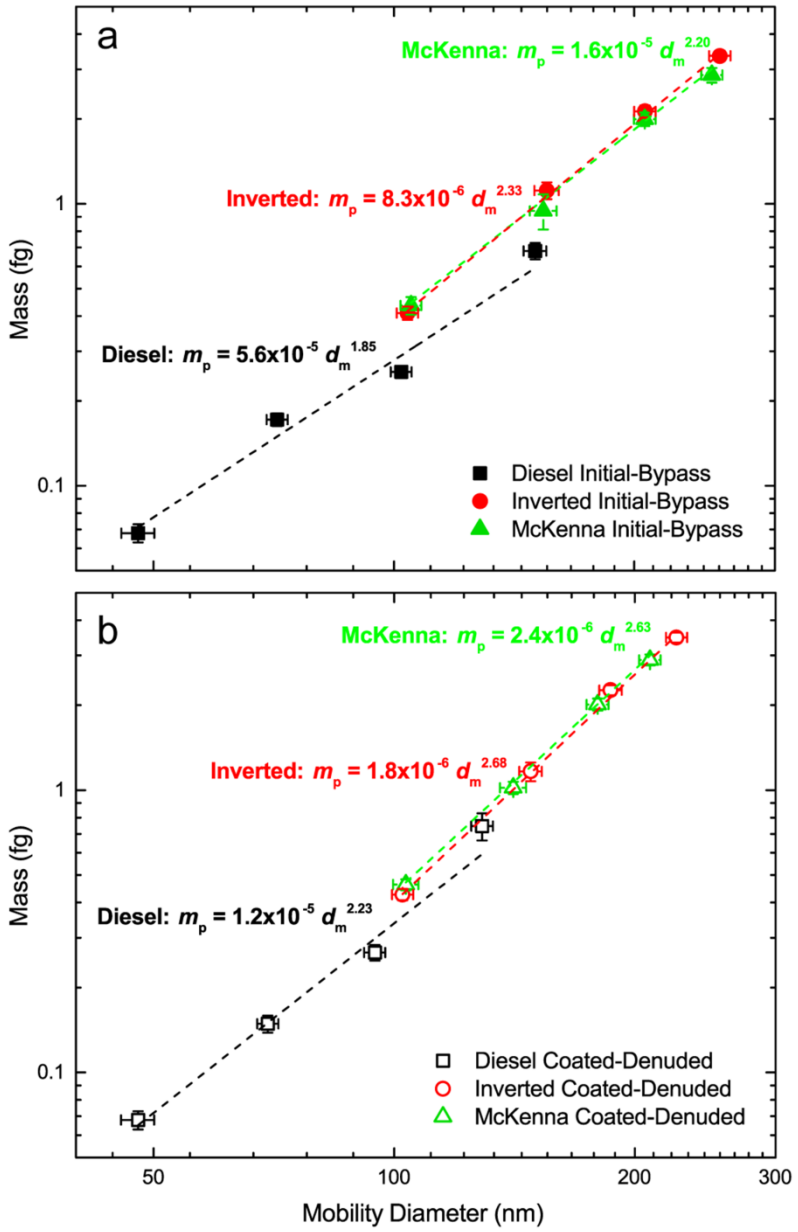

Figure 2.3. Mass-mobility relationships for soot aggregates from the three sources (a) before and (b) after restructuring. The data point at about 50 nm is the same in both plots; the mass and mobility diameter were measured directly from the diesel generator treatment train, and no photo-oxidation experiment was performed, because the number concentration after classification was too low to counteract losses to the chamber walls during injection. Since very little restructuring was observed for initially 70 nm diesel aggregates, initially 50 nm diesel aggregates are assumed to undergo no change in either mass or mobility. The constant C in the fit functions (Eq. 1) has units of $\mathrm{fg\ nm^{-D_m}}$.

mobility exponent for the inverted burner aggregates (2.33) generated at an equivalence ratio of

0.76 is the same mass-mobility exponent as that reported by Ghazi et al. for aggregates generated at an equivalence ratio of between 0.59 (Ghazi et al. 2013). At mobility diameters of 100 and 150 nm, aggregates from both burners are considerably denser than those from the diesel generator, which have a mass-mobility exponent of 1.85. The effective densities of the diesel aggregates determined here are consistent with earlier measurements (see Figure 2.4) (Olfert et al. 2007; Park et al. 2003; Maricq and Xu 2004).

The above differences in mass-mobility relationships can also be related to the diameters of the primary particles constituting the aggregates generated by each of the three sources. Primary particle diameters were investigated directly using TEM microscopy images for initially 100 nm aggregates from the three sources. The primary particles were determined using TEM microscopy for only three points because TEM analysis is time consuming, and therefore the primary particle size for other data points were performed indirectly, using mass and mobility

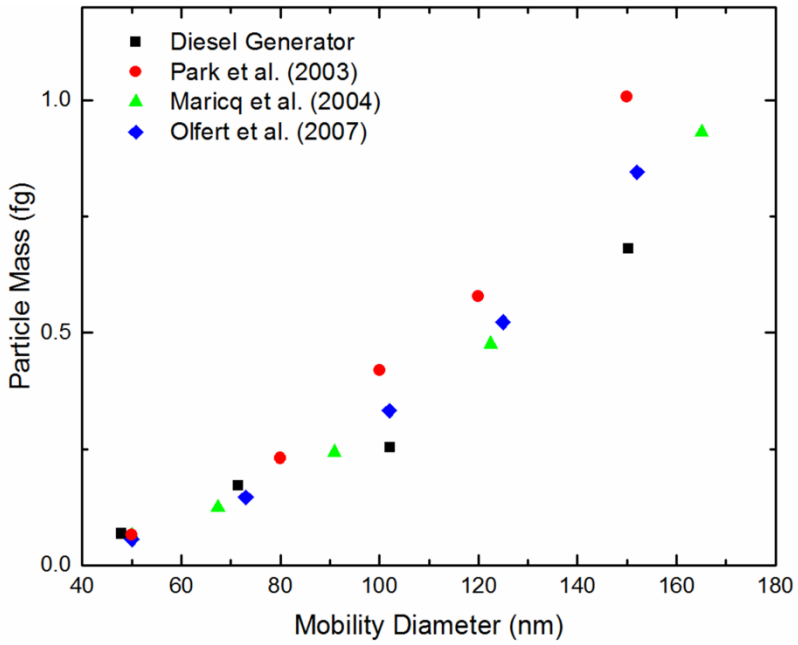

Figure 2.4. Effective densities of diesel soot aggregates from various sources (Olfert, Symonds, and Collings 2007; Park et al. 2003; Maricq and Xu 2004).

measurements. Eggersdorfer et al. has shown the relationship between the surface-area

equivalent primary particle diameter, d_{va}, can be estimated from the following relationship (2012):

$$d_{\mathrm{va}} = \left(\frac{\pi k_{\mathrm{a}} \rho}{6 m_{\mathrm{p}}} (d_{\mathrm{m}})^{2D_\alpha}\right)^{\frac{1}{2D_\alpha - 3}} \tag{2.3}$$

where $k_{\mathrm{a}}$and D_α are parameters that are determined by the type of collisions and formation of primary particles. Since zirconia particles were used in the study by Eggersdorfer et al. (2012), the reported values are not applicable to soot. Recently, Dastanpour et al. (2016b) determined the parameters for soot using mass-mobility and TEM analysis and determined the parameters as $k_{\mathrm{a}} = 1.13$ and $D_\alpha = 1.1$. Thus we estimated d_{va} values for each experiment using the values

Table 2.1. Primary particle size and number for aggregates generated by three sources and determined using indirect estimates from mass-mobility measurements and direct TEM measurements.

	Diesel Generator				**Inverted burner**				**McKenna Burner**			
	Primary Particle Size		Number of Particles		Primary Particle Size		Number of Particles		Primary Particle Size		Number of Particles	
D_{m}	Indirect	TEM	Indirect	TEM	Indirect	TEM	Indirect	TEM	Indirect	TEM	Indirect	TEM
70	26.47	-	9.82	-	-	-	-	-	-	-	-	-
100	15.61	18.01	70.33	45.81	27.04	24.50	21.89	29.41	28.55	24.63	19.86	30.91
150	18.82	-	108.56	-	31.48	-	37.90	-	26.30	-	55.09	-
200	-	-	-	-	32.25	-	67.02	-	29.59	-	80.97	-
250	-	-	-	-	31.58	-	112.89	-	27.61	-	144.18	-

determined by Dastanpour and are listed in Table 2.1, and they are compared to the *ex situ*, but direct, results of the TEM image analysis obtained by the PCM program (Dastanpour et al. 2016c). In general, the primary particles produced by the diesel generator were estimated to have smaller diameters (15.6 nm for 100 nm aggregates) than those produced by the inverted and McKenna burners (27.5 and 28.5 nm for 100 nm aggregates, respectively). Similarly, direct TEM observations of 100 nm aggregates indicate that the diesel generator produces the smallest primary particles: for the diesel generator, the mean d_{va} is 18.0 nm (with a 95% confidence interval of 13.7–22.3 nm); for the McKenna and inverted burners, the mean d_{va} values are 24.6

and 24.5 nm, respectively (with respective 95% confidence intervals of 21.8–27.4 and 21.3–27.7 nm). The average number of primary particles, N, is the ratio of aggregate mass to primary particle mass, the latter of which is derived from d_{va} and the material density of soot, and listed in Table 2.1. Based on TEM observations, aggregates initially having a 100 nm mobility diameter produced by the diesel generator comprise about 46 primary particles, whereas those produced by the McKenna and inverted burners comprise about 29 and 30 primary particles, respectively. This discrepancy explains why aggregates from the diesel generator are the least dense; the greater number of primary particles accommodates a more branched structure.

2.3.2 **Evolution of aggregate morphology.**

To generate atmospherically-relevant coatings, we exposed *p*-xylene, a representative anthropogenic aromatic hydrocarbon, to hydroxyl radical, which initiated photo-oxidation and led to the formation of semi-volatile oxygenated organic compounds. Since the concentration of hydroxyl radical was constant, the reaction of *p*-xylene was governed by pseudo-first-order kinetics, and the product concentrations increased exponentially. Once the products saturated the gas phase, they began partitioning onto the soot aggregates as SOA, leading to exponential growth in particle mass. To facilitate comparisons between aggregates from difference sources and of different initial mobility diameters, we divide mobility diameters and masses by their initial values to give diameter and mass growth factors, Gfd and Gfm, respectively. Typical trends in diameter and mass growth factors are shown in Figure 2.5-6 for initially 100 nm aggregates from both the inverted burner and the diesel generator. As shown in Figure 2.5, the

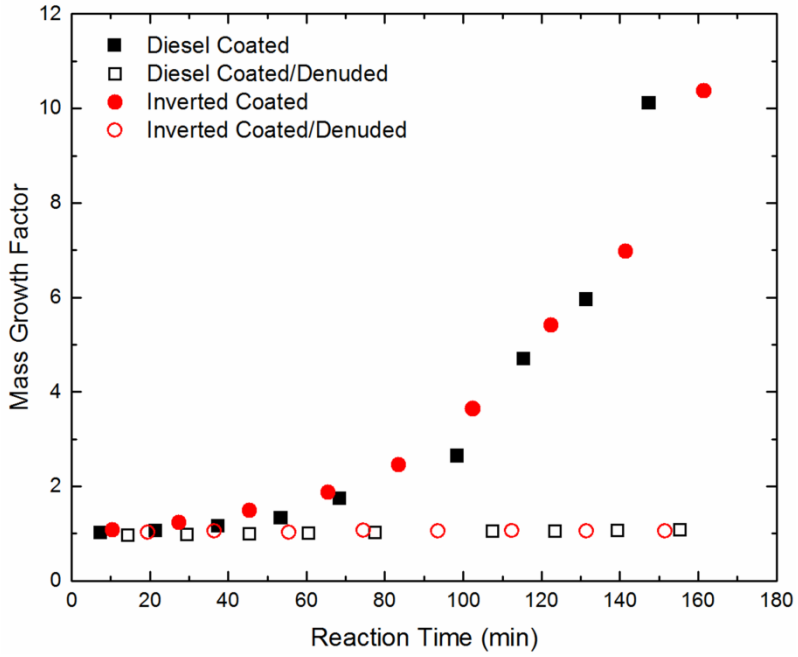

Figure 2.5. Representative time series of mass growth factors for coated and coated-denuded aggregates, initially about 100 nm in mobility diameter, generated by the inverted burner and the diesel generator.

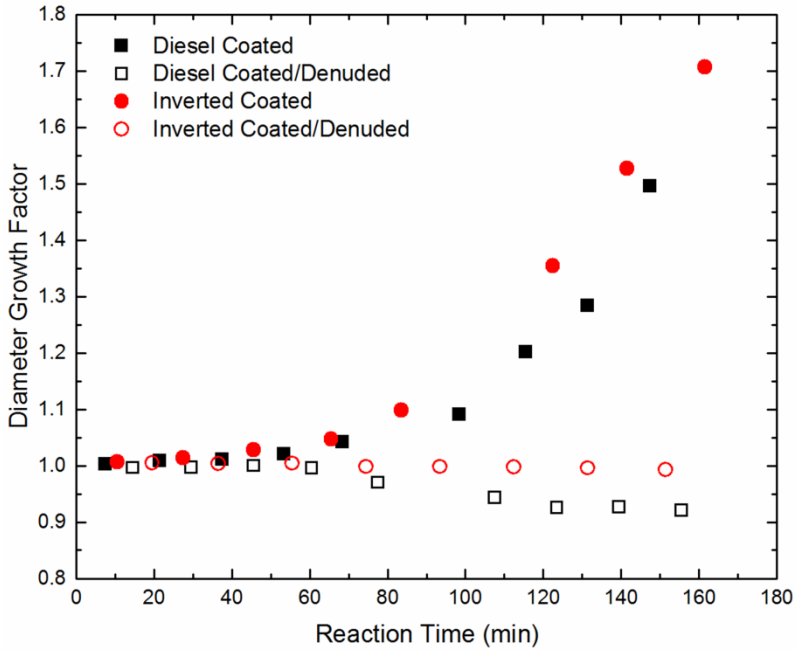

Figure 2.6. Representative time series of diameter growth factors for coated and coated-denuded aggregates, initially about 100 nm in mobility diameter, generated by the inverted burner and the diesel generator.

mass of the coated-denuded aggregates was constant throughout the experiment, indicating that

the thermo-denuder temperature (573 K) was high enough to evaporate all the SOA coating. As shown in Figure 2.6, the diameter of the coated-denuded aggregates from the generator decreased more than that of the aggregates from the burner, a first indication that the morphological evolution of soot aggregates from different sources varies.

The evolution of aggregate morphology occurs in three stages that can be identified, for example, in Figure 2.7, which depicts effective densities and shape factors versus mass growth factor for initially 250 nm aggregates from the two burners. In the first stage, the coated particles increase in effective density as coating mass increases, but the effective density of the coated-denuded aggregates remains relatively steady, indicating that the core soot aggregates retain their initial morphologies. This induction period is not captured by an earlier exponential model derived from experiments with a lower coating mass resolution (Ghazi and Olfert 2013). In the second stage, commencing at a mass growth factor of about 1.5, the soot aggregates begin to restructure under the influence of the SOA coating. The final stage commences at a mass growth factor of about five, and the effective density of the coated-denuded soot plateaus at approximately 0.6 g cm^{-3}, which is considerably lower than the material density of soot. The shape factors of the coated particles continue to decrease with increasing coating mass before reaching unity at a mass growth factor of approximately 10, indicating that a thickly-coated spherical particle is then present. Despite the initial difference in the shape factors of the coated-denuded aggregates from the two burners, they both plateau at approximately 1.8, which implies that the restructured soot is not spherical, consistent with the final effective density.

In order to determine the effective density of the SOA coating used in these experiments, significantly greater coating masses were applied to initially 150 nm aggregates from the inverted burner. As shown in Figure 2.8 a mass growth factor of over 30 is reached. As discussed

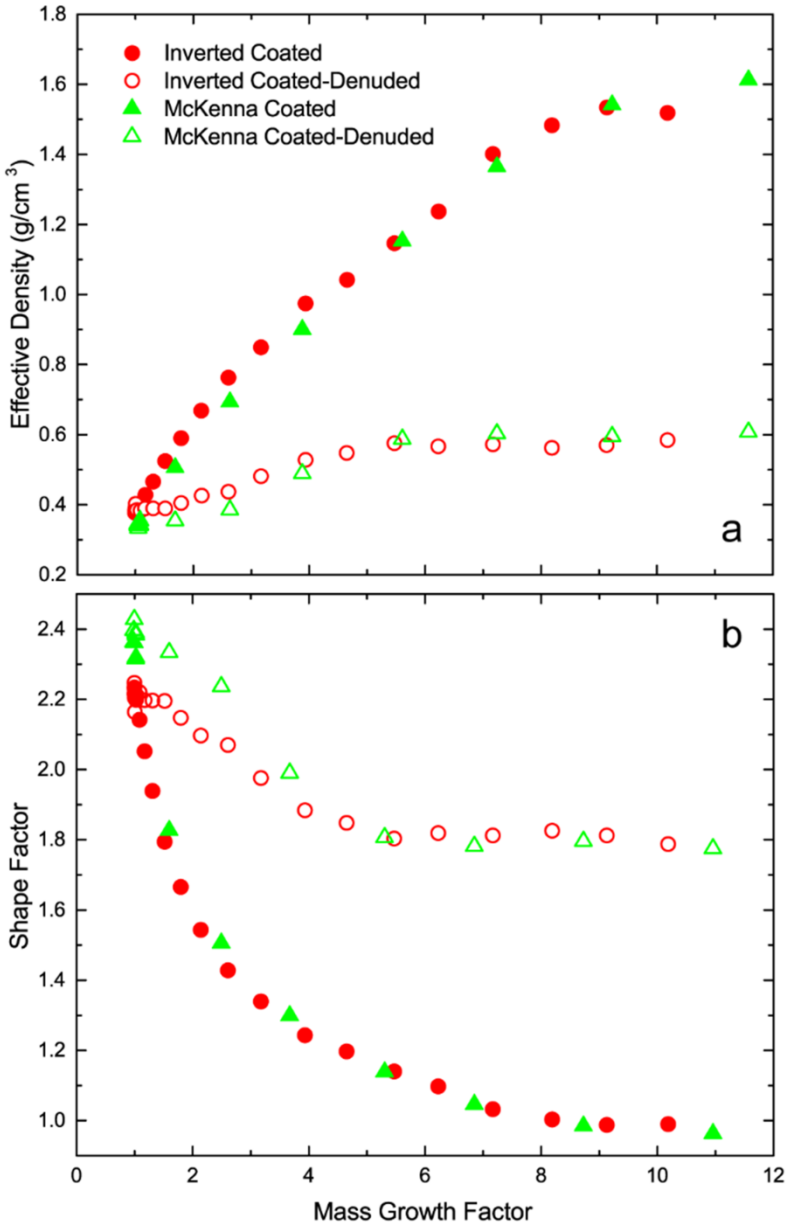

Figure 2.7. Trends in (a) effective density and (b) shape factor with increasing mass growth factor for coated and coated-denuded burner-generated aggregates initially about 250 nm in mobility diameter.

above, at a mass growth factor of approximately 10, the shape factor of the coated particles plateau, and the effective density ceases to increase. As the mass growth factor continues to increase, the shape factor is of course constant, but the effective density exhibits a slight decrease, because the mass fraction of the soot, which is denser than the SOA coating, decreases

significantly. The asymptote corresponds to the material density of the SOA coating, an material density of approximately 1.4 g cm^{-3}.

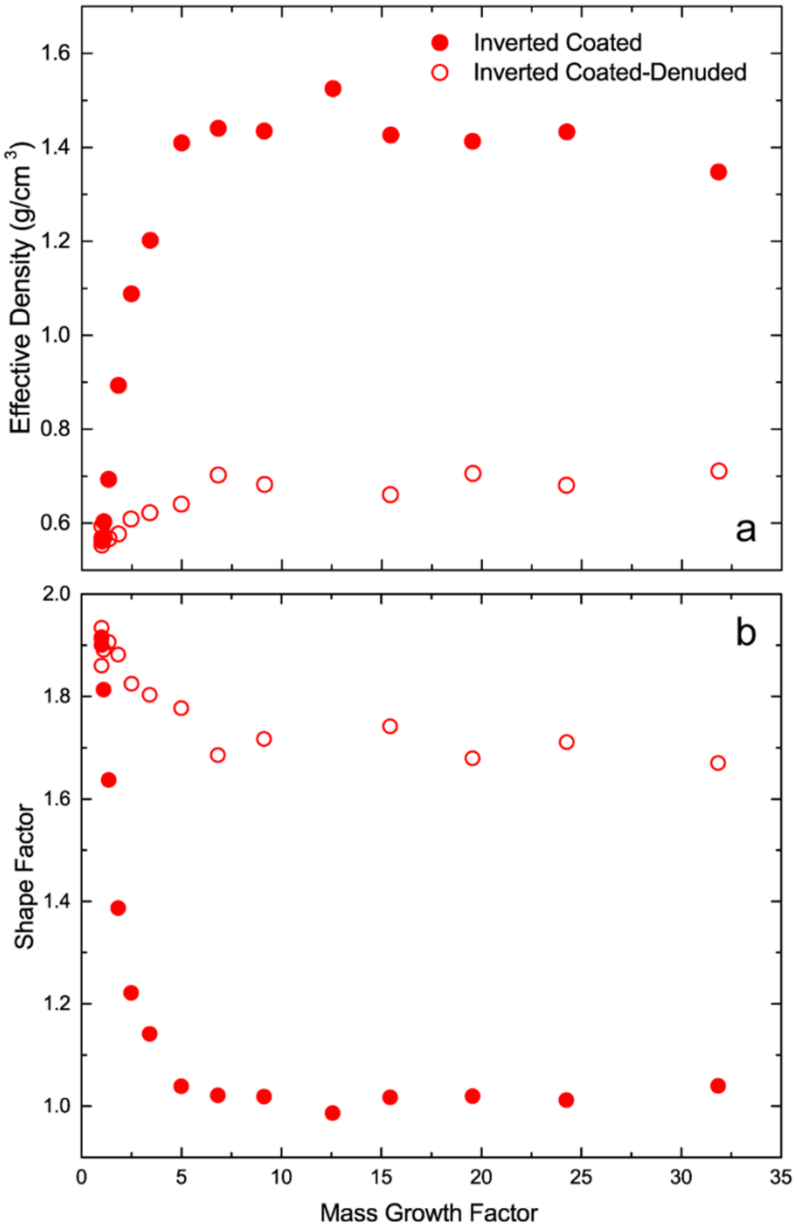

Figure 2.8. Trends in (a) effective density and (b) shape factor with increasing mass growth factor for coated and coated-denuded aggregates, initially about 150 nm in mobility diameter, generated by the inverted burner.

To compare the evolution of soot aggregates from all three sources, we must consider smaller aggregates, because too few 250 nm aggregates are produced by the diesel generator to

allow classification and injection into the smog chamber. Accordingly, trends in effective densities and shape factors versus mass growth factor are shown in Figure 2.9 for initially 100 nm aggregates from the three sources. As noted above for the 250 nm aggregates, restructuring began at a mass growth factor of about 1.5. For aggregates from the two burners, restructuring

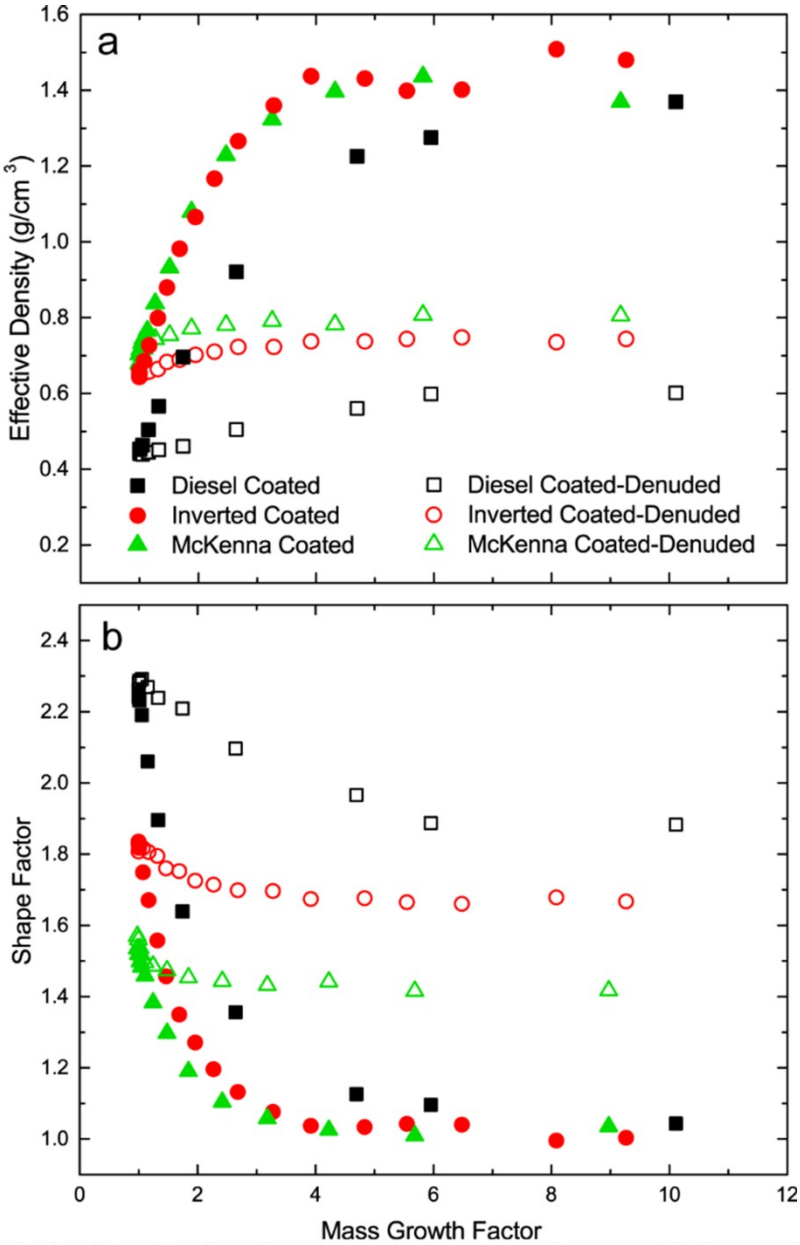

Figure 2.9. Trends in (a) effective density and (b) shape factor with increasing mass growth factor for coated and coated-denuded aggregates, initially about 100 nm in mobility diameter, generated by all three sources.

continued until the mass growth factor reached about three, at which point the effective densities and shape factors of the coated-denuded particles plateaued. In contrast, for aggregates from the diesel generator, restructuring continued until the mass growth factor reached approximately six. The initial effective densities of aggregates from the McKenna and inverted burners are similar (~ 0.6 g cm^{-3}), whereas that of the aggregates from the diesel generator is lower (~ 0.4 g cm^{-3}). Despite the difference in initial effective densities, the coated diesel aggregate effective density increase less rapidly to approximately 1.4 g cm^{-3} than those of the other aggregates. When restructuring is complete, the coated-denuded aggregates from the McKenna and inverted burners reach effective densities of approximately 0.75 g cm^{-3}, while the diesel aggregates plateau at an effective density of 0.6 g cm^{-3}. The shape factors of the coated aggregates from the burners converge to unity at a mass growth factor of approximately four, while that of the diesel aggregates converge at mass growth factors closer to 10.

Despite the above differences between 100 nm aggregates from the burners and the diesel generator, the evolution of initially 100 nm aggregates from the diesel generator is remarkably similar to that of initially 200 nm aggregates from the burners, as depicted in Figure 2.10. In both cases, aggregates cease restructuring at a mass growth factor of six, and coated particles reach sphericity at a mass growth factor of about 10. Interestingly, the 100 nm diesel aggregates and 200 nm inverted burner aggregates comprise similar numbers of primary particles, 70 and 67, respectively (see Table S1), suggesting that restructuring is related to primary particle number. This notion is explored in greater detail below.

2.3.3 **Final aggregate morphology.**

The compaction of coated-denuded aggregates can be visualized using representative TEM samples collected before and after the photo-oxidation stage of a typical experiment,

shown in Figure 2.11a-b for initially 100 nm inverted burner aggregates. As shown in Figure 2.12, the final mobility diameter ratio, the ratio of the final restructured aggregate mobility diameter to the initial aggregate mobility diameter, decreases for all three sources as a function of initial mobility diameter. However, at a given initial mobility diameter, the degree of

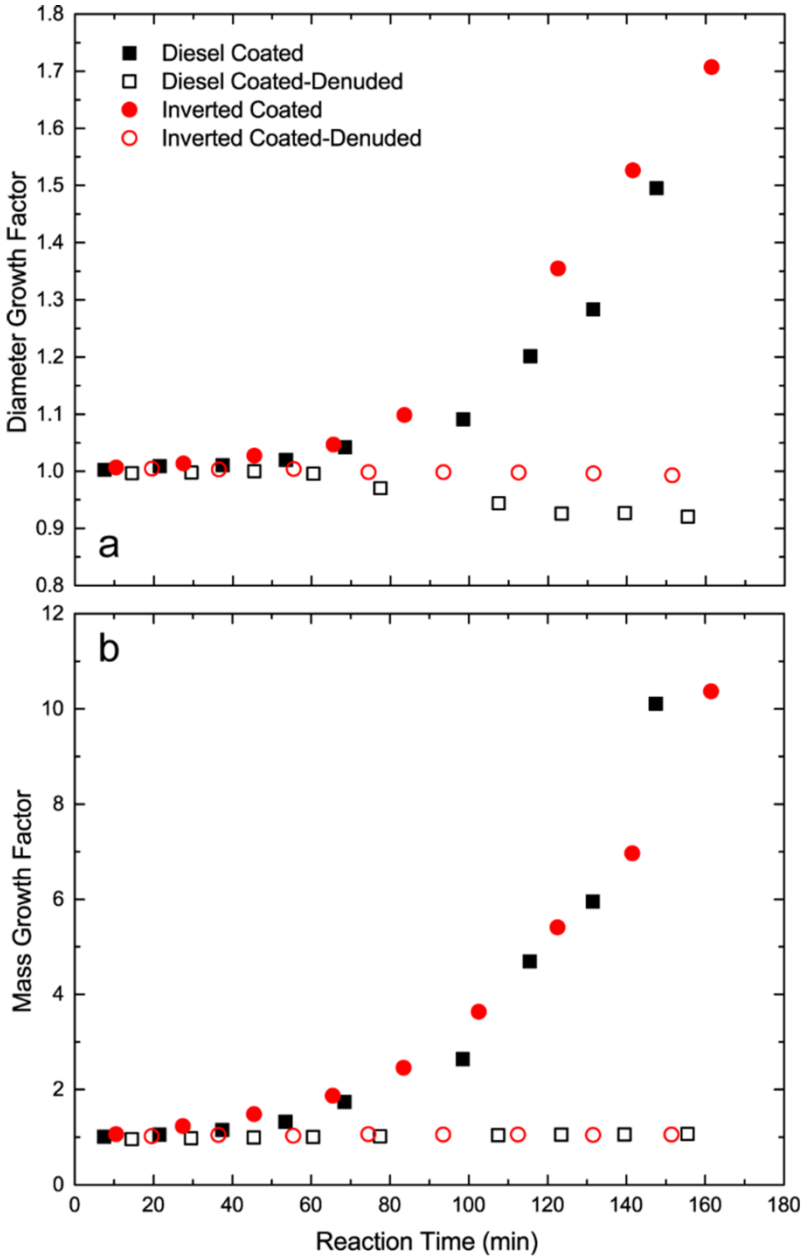

Figure 2.10. Representative time series of (a) diameter and (b) mass growth factors for coated and coated-denuded aggregates, initially about 100 nm in mobility diameter, generated by the inverted burner and the diesel generator.

restructuring varies significantly with the source of the soot. For example, at an initial mobility diameter of about 100 nm, aggregates from the diesel generator collapse appreciably (Gfd = 0.92), but those from the burners do not (Gfd = 0.99). Diesel and inverted burner aggregates initially 100 nm in mobility diameter comprise about 70 and 22 primary particles, respectively; these estimates, based on the indirect method described above (see Eq. 2.3), suggest that in general an aggregate comprised of more primary particles accommodates more restructuring. If we compare initially 100 nm diesel aggregates and initially 200 nm inverted burner aggregates, as above, there is a striking similarity between the final mobility diameter ratios (0.92 compared to 0.90) and primary particle numbers (70 compared to 67).

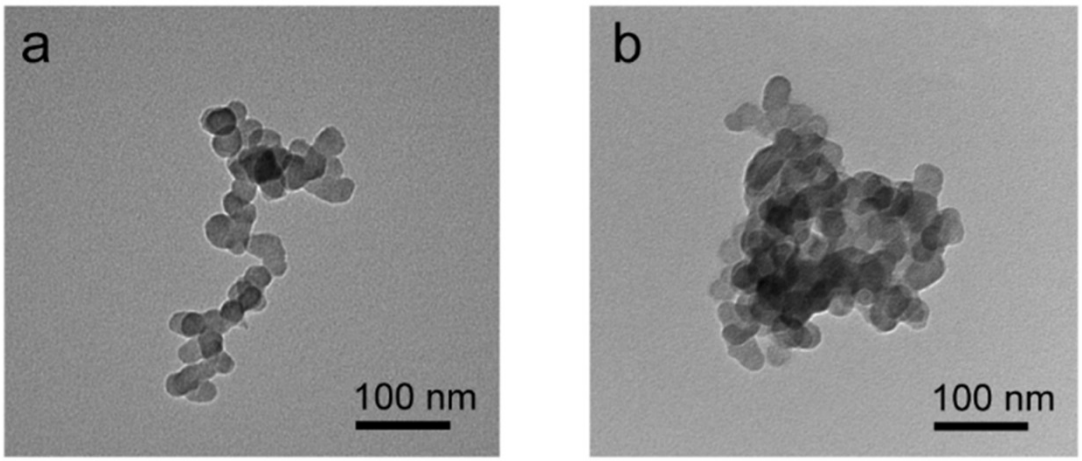

Figure 2.11. TEM images of initially 100 nm inverted burner soot aggregates (a) before and (b) after restructuring due to SOA coating.

Motivated by the above comparisons between aggregates comprising roughly the same number of primary particles, we consider here whether there is a systematic relationship between the final degree of restructuring and primary particle number. Remarkably, a plot of the final mobility diameter ratio as a function of the number of primary particles per aggregate (see Figure

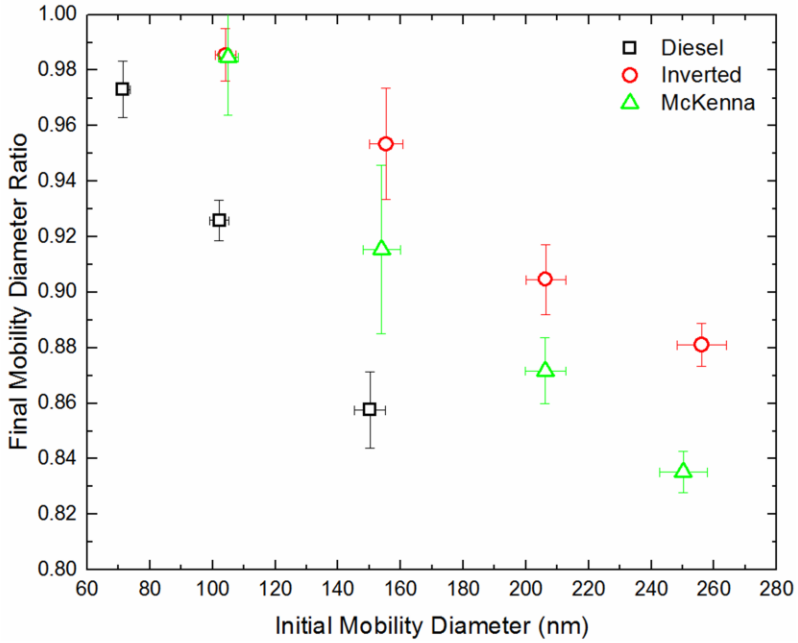

Figure 2.12. The final diameter growth factor as a function of initial mobility diameter.

2.13) reveals a linear relationship across the range most relevant to ambient soot. If separate fits are performed for each source, all three are nearly identical, indicating that the source of the soot is important only to the extent that it dictates the size and number of primary particles. Furthermore, aggregates with similar numbers of primary particles collapse to a similar extent at any given coating ratio, even before reaching the final morphology; for example, at mass growth factor of about five, 100 nm diesel aggregates and 200 nm inverted burner aggregates both collapse by about 6% of their initial mobility diameters. Consequently, if modelers know only the number of primary particles per aggregate for a given ambient sample, which can be derived from mass-mobility relationships that are known for many types of soot (Ghazi et al. 2013; Dastanpour et al. 2016b), and the coating mass, they can predict the evolution of aggregate morphology and, in turn, may be able to make better estimations of the evolution of the optical properties of soot aggregates (Wu et al. 2017).

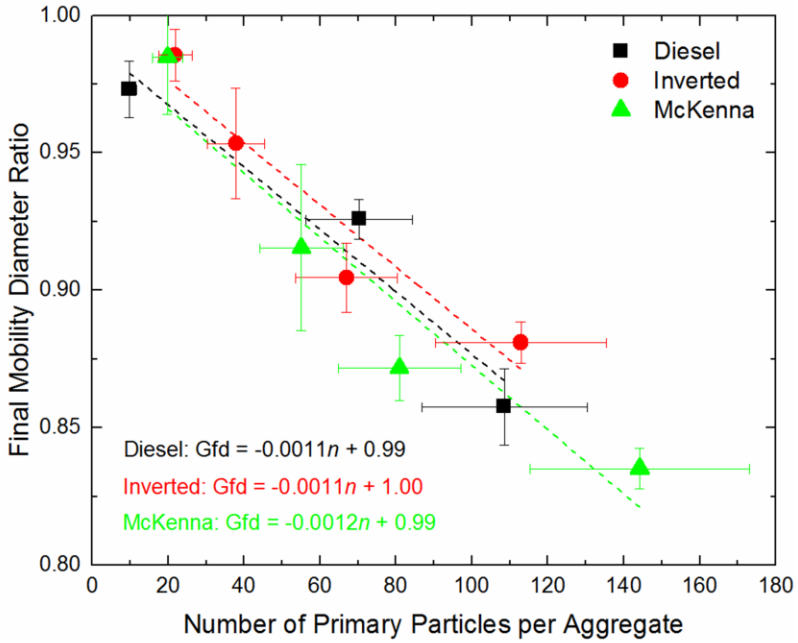

Figure 2.13. The final diameter growth factor as a function of the number of primary particles per aggregate, estimated using the indirect method; the relative uncertainty in the number of primary particles is 20% (Dastanpour et al. 2016).

We note that the final coated-denuded aggregates from the three sources were not spherical. Consider the final mass-mobility exponents of aggregates from the McKenna burner, inverted burner, and diesel generator, as shown in Figure 2.3b: 2.63, 2.68, and 2.23, respectively. These values are significantly greater than the initial mass-mobility exponents (2.20, 2.33, and 1.85, respectively), but they are still well below three, indicating that indeed these aggregates were non-spherical when restructuring ceased. Further restructuring could occur if the surface tension of the coating increased; for example, coatings of glycerol (64 mN m^{-1} at 20 °C) have been shown to result in final mass-mobility exponents of three for aggregates generated by the McKenna burner (Schnitzler et al. 2017). Consequently, the linear relationships reported here, although accurate for the representative anthropogenic SOA coating, could change for coatings of higher surface tension. In the atmosphere, the surface tension of SOA may increase via water uptake at high relative humidity (Lee and Hildemann 2014). Furthermore, photo-chemical aging

and the attendant increase in the oxygen-to-carbon ratio of the SOA, may also increase the surface tension and will certainly increase the hygroscopicity (Massoli et al. 2010).

Chapter 3.

Relative Humidity Dependence of Soot Aggregate Restructuring Inducted by Secondary Organic Aerosol: Effects of Water on Coating Viscosity and Surface Tension

3.1 **Introduction**

Soot aggregates are composed of primary particles of elemental carbon, and they are generated, for example, from the combustion of hydrocarbon fuels (Olfert et al. 2007; Park et al. 2003) and biomass (Keywood et al. 2013; Schwarz et al. 2008). Since elemental carbon strongly absorbs all visible wavelengths of light, soot aggregates have a significant warming effect on global climate (Bond and Bergstrom 2006; Bond et al. 2013). During combustion, incipient primary particles undergo random Brownian motion and collide with other primary particles to form branched, fractal-like aggregates (Sorensen 2011). The aggregates can become more compact through restructuring caused by internally-mixed liquids, such as water (Mikhailov and Vlasenko 2007; Pagels et al. 2009; Miljevic et al. 2012) and sulfuric acid (Pagels et al. 2009; Khalizov et al. 2009). Soot aggregate restructuring due to liquid coatings has been shown to depend on the coating mass (or volume) (R. Ghazi and Olfert 2013) and surface tension, σ (Schnitzler et al. 2017). The morphological evolution of soot aggregates affects their optical properties, which have been investigated both experimentally (Radney et al. 2014; Xue et al. 2009; Cappa et al. 2012) and theoretically (Liu et al. 2016; Wu et al. 2017).

In the atmosphere, soot aggregates may be coated by mixtures of many species. Secondary organic aerosol (SOA) - generated from the photo-oxidation of biogenic and anthropogenic volatile organic compounds (VOCs), consisting of many semi-volatile oxygenated

organic species (Mentel et al. 2009; Donahue et al. 2006). In the laboratory, soot aggregate restructuring has been induced by coatings of SOA derived from both biogenic (isoprene (Khalizov et al. 2013) and α-pinene (Schnaiter 2005; Saathoff et al. 2003)) and anthropogenic (benzene (Schnitzler et al. 2014), toluene (Schnitzler et al. 2014; Qiu et al. 2012), ethylbenzene (Schnitzler et al. 2014), and *m*- and *p*-xylene (Schnitzler et al. 2017; Schnitzler et al. 2014; Guo et al. 2016)) VOCs. Recently, the viscosity of SOA derived from isoprene and toluene has been shown to vary significantly with relative humidity (RH) (Song et al. 2016; Song et al. 2015); for example, when poked with a needle, toluene-derived SOA, collected in a large droplet on a slide, shatters at 16.5% RH but returns to its original shape at 39.5% RH, with a characteristic flow time (Song et al. 2016). If an SOA coating is a solid at a certain temperature and RH, it would not be expected to restructure soot aggregates under these conditions. In previous studies, SOA-coated soot has been investigated at only low ($\leq$ 20%) and high (90%) RH (Khalizov et al. 2013; Schnitzler et al. 2014; Qiu et al. 2012; Guo et al. 2016). Studies at intermediate RHs are necessary to fully understand the effects of water on SOA coating mass, viscosity, and surface tension, and their bearing on SOA-induced soot aggregate restructuring.

Here, we report smog chamber experiments in which mono-disperse soot aggregates, generated by ethylene combustion in a McKenna premixed burner, were coated with *p*-xylene SOA and then exposed to a controlled RH. Particle diameter and mass were monitored using a differential mobility analyzer (DMA; TSI, 3081) and a centrifugal particle mass analyzer (CPMA; Cambustion), respectively. Trends in humidified mobility diameter with dry particle mass were evaluated to determine how RH affects SOA viscosity and surface tension and, in turn, SOA-induced soot aggregate restructuring.

3.2 **Experimental Section**

Soot aggregates were generated by a McKenna premixed burner, in which ethylene was used as fuel. The experimental setup for treatment and injection of soot is depicted in Figure 3.1a, and it is similar to that used in chapter 2. The equivalence ratio of the burner was set to two, using ethylene and air flow rates of 1.1 and 8.0 L min^{-1}, respectively. Soot was sampled 27 cm above the flame and fed into an ejector dilutor (Air-Vac, AVR038H), which was

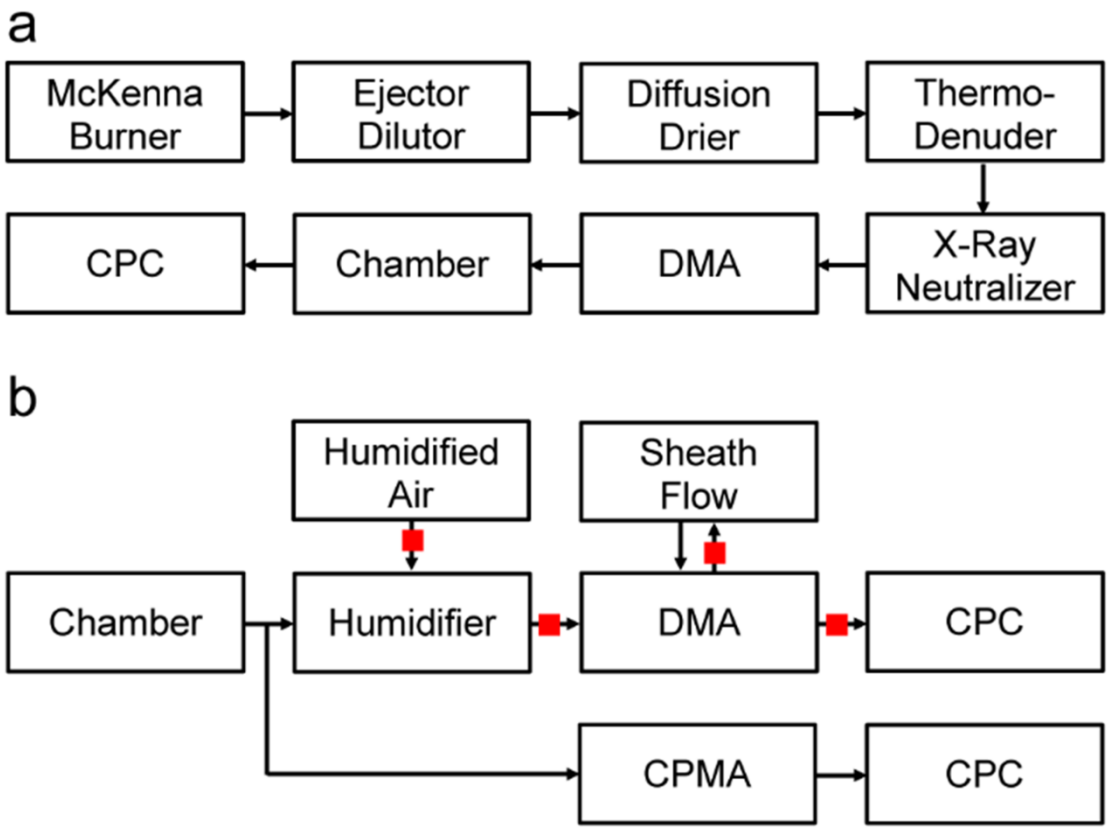

Figure 3.1. Experimental setup during soot aggregate (a) treatment and injection and (b) photo-oxidation and sampling. Red squares denote RH and temperature probes. DMA: differential mobility analyzer; CPC: condensational particle counter; CPMA: centrifugal particle mass analyzer.

set to a dilution ratio of three, using 210 kPa of nitrogen. As discussed in chapter 2, the ejector dilutor was used to sample soot from the burner while reducing the water vapour in the sample line. The aggregates were then passed through a diffusion drier and a thermo-denuder set to 573 K to remove trace gases.

After treatment, the soot aggregates were neutralized using an X-ray source (TSI, 3087) and directed into a DMA, which was set to classify predominantly singly-charged particles 250 nm in mobility diameter, at sample and sheath flow rates of 1.0 and 10.0 L min^{-1}, respectively. The classified aggregates were then injected into a smog chamber, as described in chapter 2. A deuterium lamp (Ocean Optics, D-2000-S) and a spectrometer (Ocean Optics, HR 2000+) were used to measure *p*-xylene concentrations by differential optical absorption spectroscopy (Parsons et al. 2011).

Once the soot aggregate injection was completed (typically, at a particle concentration > 1000 cm^{-3}), aggregates were sampled from the chamber into parallel DMA-condensation particle counter (CPC; TSI, 3776) and CPMA-CPC (TSI, 3771) systems. Soot aggregates were monitored for approximately one hour after injection to confirm there was no background change in mobility diameter or mass before *p*-xylene (Fisher, 99.9%) was injected into the chamber to a concentration of ~2 ppm. Hydrogen peroxide (Sigma, 30% w/w in water) was then injected into the chamber, and UV radiation was applied to produce hydroxyl radicals. Though water was introduced along with hydrogen peroxide, the chamber RH was $< 12\%$ throughout each experiment. In all experiments, the CPMA was operated at the chamber RH; in contrast, the DMA was operated at different controlled RHs: $< 12\%$, 20%, 40%, 60%, and 85% at operating temperatures ranging from 23 to 25 °C. For each experiment at RH $\geq 20\%$, the DMA sample was conditioned by a Nafion membrane humidifier (Perma Pure, PD-625-24SS). The RH in the conditioning train and DMA was monitored using a series of RH and temperature probes (Sensirion, SHT75), placed as shown in Figure 3.1b.

3.3 **Results and Discussion**

To facilitate comparisons between experiments, the measured mobility diameters and masses are divided by their initial values to give normalized diameter and mass growth factors, Gfd and Gfm, respectively. Trends in Gfd with increasing Gfm are plotted in Figure 3.2. At each RH, two different sample flow rates, 0.3 and 1.5 L min^{-1}, of the DMA were used to vary the

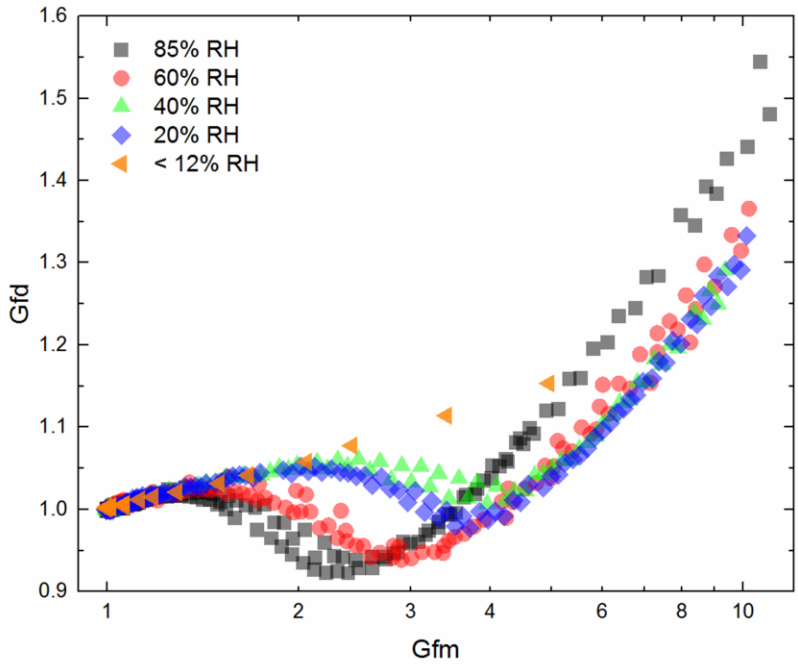

Figure 3.2. RH-dependent trends in diameter growth factor with increasing mass growth factor, which reflect the morphological evolution of the soot aggregates during photo-oxidation.

residence time of the aggregates in the RH-controlled conditioning train. Despite small discrepancies, reflected in the scatter in Figure 3.2, no systematic dependence of the aggregate evolution on the residence time was observed. Therefore, trends in Gfd measured at both flow settings, distinguished only by RH, are shown in Figure 3.2. At RH < 12%, Gfd increases uniformly with Gfm, suggesting that there is little or no soot aggregate restructuring to compensate for the coating thickness.

At RH ≥ 20%, the evolution of aggregate morphology occurs in three stages. In the first stage, the Gfd increases slightly with Gfm indicating that SOA only thinly coats the soot

aggregates while they retain their initial structures.. During the second stage, the Gfd decreases as Gfm increases, indicating that the effects on mobility diameter due to aggregate restructuring under the influence of the SOA coating now outweigh the effects of SOA coating. At RHs of 20 and 40%, the decrease in Gfd begins at a Gfm between two and three, leading to a local minimum in Gfd of about unity; at RHs of 60 and 85%, the decrease in Gfd begins at a smaller Gfm, ~1.5, leading to a local minimum in Gfd of ~0.95. In the third stage, the Gfd again increases with Gfm, suggesting that aggregate restructuring is no longer significant enough to outweigh the contribution of the coating to the mobility diameter.The Gfm at which this stage begins also depends on RH; at RHs of 20 and 40%, the third stage begins at a Gfm of about four, and at RHs of 60 and 85%, it begins at a Gfm between two to three.

These differences reveal a significant dependence of aggregate evolution on RH. In the past, SOA-induced restructuring of soot aggregates was investigated at RHs of ≤ 20 and 90% (Schnitzler et al. 2014; Qiu et al. 2012; Guo et al. 2016), and water was shown to be important only to the extent that it increased the coating mass (or volume) (Qiu et al. 2012). Here, by investigating intermediate RHs, we demonstrate that water is important also for its effects on the viscosity and surface tension of the coatings. These effects are discussed in the context of Figure 3.3 which shows the evolution in shape factor, χ, with increasing Gfm. The dynamic shape factor is a correction parameter to account for the increased drag experienced by an irregular shape particle relative to its spherical equivalent (volume or mass). This parameter is added because irregular shaped particles have a greater surface interaction with the gas/fluid than its volume/mass equivalent spherical counterpart (DeCarlo et al. 2004). By definition, the shape factor is the ratio of particle resistance force to the resistance force of a sphere having the same volume and relative velocity (Hinds 1999). The shape factor is calculated as $[d_{\mathrm{m}} C_{\mathrm{c}}(d_{\mathrm{ve}})]/$

$[d_{ve}C_c(d_m)]$, where C_c is the slip correction, and d_{ve} is the volume-equivalent diameter, calculated as

$$d_{ve} = \left[\frac{6}{\pi}\left(\frac{m_{soot}}{\rho_{soot}} + \frac{m_p - m_{soot}}{\rho_{SOA}}\right)\right]^{\frac{1}{3}} \quad (3.1)$$

where m_{soot} is the mass of the soot aggregates after injection and before photo-oxidation, m_p is the combined mass of the aggregates and coatings during photo-oxidation, and ρ_{soot} and ρ_{SOA} are the material densities of soot and *p*-xylene SOA, 1.8 and 1.46 g cm^{-3}, respectively. Initially, the aggregates have a shape factor of ~2.4, which begins to decrease as Gfm increases.

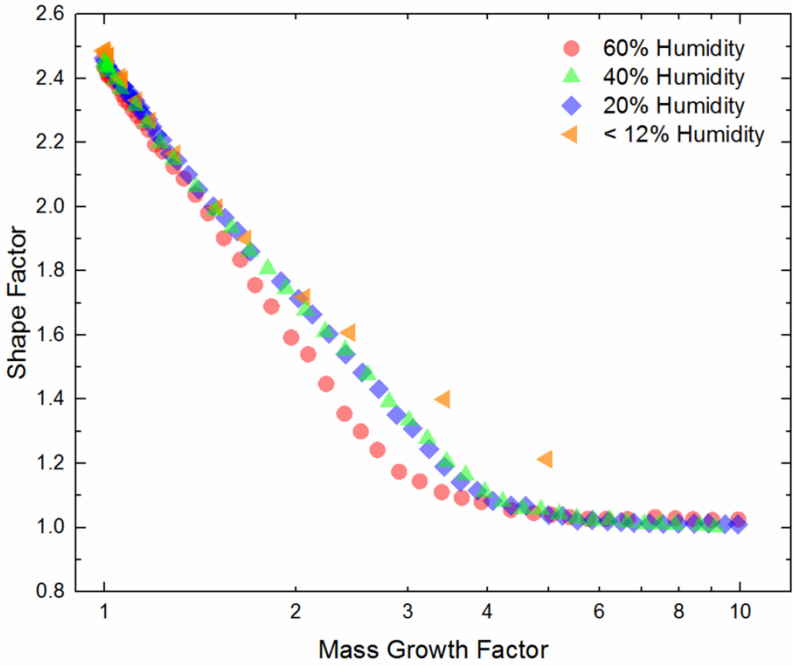

Figure 3.3. RH-dependent trends in shape factor with increasing mass growth factor.

First, we consider the experiment at RH < 12%. Since toluene SOA, collected in a large droplet on a slide, was observed to shatter when poked at 16.5% RH and not flow at all after 6.5 h of observation (Song et al. 2016), the *p*-xylene SOA is assumed to be a solid at RH < 12%. Consequently, it is too viscous to induce restructuring, consistent with the uniformly increasing Gfd noted above. Thus, the decrease in shape factor shown in Figure 3.3 results solely from

accumulation of the SOA coating that would lead eventually, at a Gfm of about eight (Schnitzler et al. 2014), to a spherical particle encapsulating the unchanged soot aggregate. In earlier experiments performed at low RH, Gfd also increased uniformly with SOA coating mass (or thickness) (Schnitzler et al. 2014; Qiu et al. 2012); nonetheless, restructuring was inferred from a decrease in mobility diameter upon thermo-denuding the coated aggregates (Schnitzler et al. 2014; Qiu et al. 2012). Our results indicate that the restructuring observed for coated-denuded particles likely occurred in the thermo-denuder, where the elevated temperature caused the viscosity of the SOA coatings to decrease. These results also relate to a recent estimation of SOA surface tension, based on the extent of soot aggregate restructuring, because an increase in temperature corresponds to a decrease in surface tension (Schnitzler et al. 2017). We stress that, regardless of the RH, the restructuring occurs while the coating is still present; if restructuring occurred during coating evaporation, the Gfd would not decrease at any RH (see Figure 3.2). Similarly, decreases in Gfd were observed for aggregates thinly-coated with pure liquids, including sulfuric acid and oleic acid (Pagels et al. 2009; Ghazi and Olfert 2013). In contrast, light scattering by aggregates injected into bulk water implied that the aggregates did not restructure without coating evaporation (Ma et al. 2013).

At RH $\geq$ 20%, soot aggregate restructuring without denuding is unambiguous, because Gfd decreases in the second stage of aggregate evolution, described above. That there is no dependence on residence time in the RH-controlled conditioning train indicates that, at both flow rates, the soot-coating interface reaches equilibrium. At the high flow rate (1.5 L min^{-1}), the residence time in the conditioning train is about 15 s, which is comparable to the experimental flow time of toluene SOA measured by Song et al. at 40% RH (τ = 13.75 s) (Song et al. 2016). On the other hand, the residence time is significantly less than the flow time measured by Song

et al. at their lowest RH (30%), which was on the order of 10^3 s (Song et al. 2016). At RHs of 20 and 40%, the extent of soot aggregate restructuring is similar, indicated by their overlapping trends in shape factor with Gfm in Figure 3.3. The Gfm required for the shape factor to converge to unity decreases from eight to about five, because the encapsulated soot core itself is more compact. At 60% RH, the role of restructuring increases, such that shape factor decreases towards unity even more sharply. At both RHs of 40 and 60%, the soot-coating interfaces have enough time to reach equilibrium, so the difference in extent of restructuring must be due to a difference in the surface tensions of the coatings. Since coatings of higher surface tension result

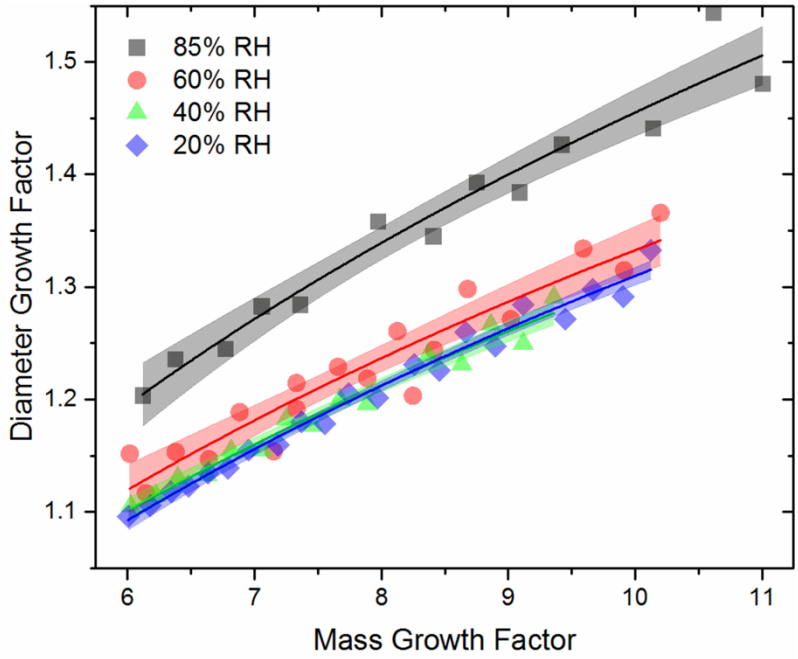

Figure 3.4. Logarithmic fits to data at mass growth factors between 6 and 11, at which the coated aggregates are spherical, used to determine the diameter growth factor at a mass growth factor of exactly 8.5 for each experiment at RH ≥ 20%. The filled regions about the curves depict the 95% confidence intervals. The adjusted R^2 values range from 0.90 (at 60% RH) to 0.98 (at 20% RH).

in a greater extent of restructuring (Schnitzler et al. 2017), the SOA coating likely has a greater surface tension at 60% RH than at 40% RH.

This difference suggests appreciable water uptake at RH ≥ 60%. The values of Gfd shown in Figure 3.2 are derived from diameters measured downstream of the RH-controlled conditioning train, so they include contributions from soot, SOA, and any condensed water. In contrast, the values of Gfm are derived from masses measured upstream of the conditioning train, so they include contributions from only soot and SOA. By design, this arrangement prevented partial evaporation of any condensed water in the CPMA, where temperature fluctuates periodically with rotational speed. As a result, the values of Gfd at all RHs do not converge at high Gfm. For spherical particles, the differences in Gfd can be used to quantify the volume of particle-bound water. Measurements at a Gfm > 6 were used to fit logarithmic curves,

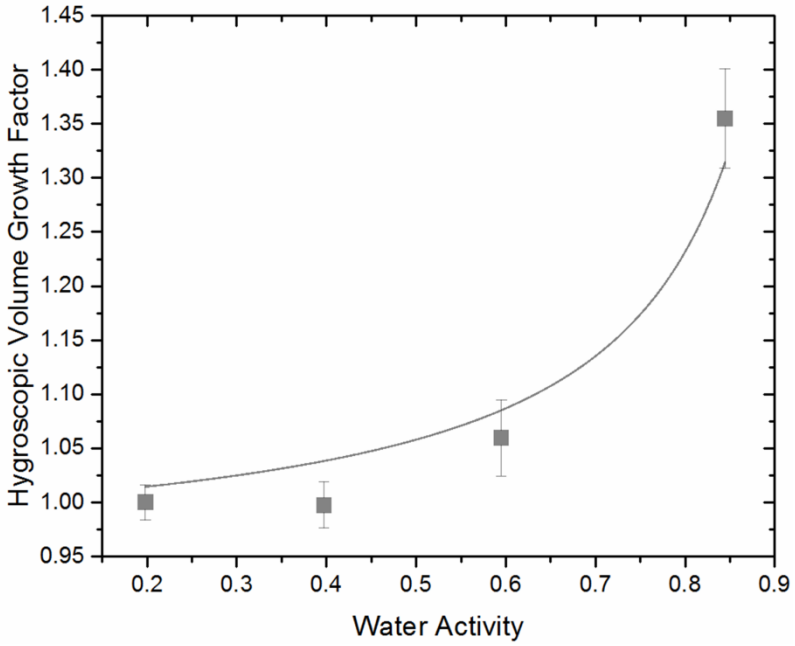

Figure 3.5. The hygroscopic volume growth factors of spherical SOA-coated soot aggregates at a mass growth factor of 8.5 as a function of water activity. In the fit of Equation 3.2, the data points are weighted per the error bars in the *y*-axis, which are calculated by propagation of error from the 95% confidence intervals shown in Figure 3.4

as shown in Figure 3.4, from which the respective values of Gfd at a Gfm of exactly 8.5 were calculated. $Gfd_{20\%}$ is assumed to be that of only soot and SOA. For higher RHs, the hygroscopic diameter growth factor, hGfd, is calculated as $Gfd_{RH}/Gfd_{20\%}$; in turn, the hygroscopic volume

growth factor, hGfv, is calculated as $(\text{hGfd})^3$. The values of hGfv at RHs 20-85% are shown in Figure 3.5. RH was converted to water activity, a_{w}, to account for the Kelvin effect.

A single-parameter hygroscopicity model relates hGfv to the activity of water (Kreidenweis et al. 2008; Petters and Kreidenweis 2007), as follows:

$$\text{hGfv} = \frac{v_{\text{soot}} + v_{\text{SOA}} + v_{\text{w}}}{v_{\text{soot}} + v_{\text{SOA}}} = \kappa\left(\frac{a_{\text{w}}}{1 - a_{\text{w}}}\right) + 1 \tag{3.2}$$

where v_{soot}, v_{SOA}, and v_{w} are the volumes of soot, SOA, and particle-bound water, respectively, and κ is the hygroscopicity parameter. A fit of Equation 3.2 to the data in Figure 3.5 results in a κ value of 0.058 for the SOA-coated aggregates. This value was used to calculate the total mass of the particles (soot, SOA, and water) for the duration of the 85% RH experiment and to plot Gfd versus total Gfm (see Figure 3.6). Since soot is hydrophobic, $\kappa_{\text{soot}} = 0$, and division of κ by the volume fraction of SOA (0.91) at a Gfm of 8.5 gives κ_{SOA} of 0.063. Accounting for the standard error in the fit, κ_{SOA} is 0.06±0.01. This value is comparable to that of phthalic acid, 0.059 (Petters and Kreidenweis 2007; Huff Hartz et al. 2006), which is similar to the ring-retaining products of *p*-xylene photo-oxidation (Forstner et al. 1997). Furthermore, our value falls among those recently reported for SOA particles derived from mixtures of biogenic and anthropogenic precursors, which had an oxygen-to-carbon ratio, O:C, of about 0.5-0.6 (Zhao et al. 2016). On the other hand, our value is lower than the 0.09-0.10 range recently reported for SOA particles derived from anthropogenic precursors (including benzene, toluene, and *p*-xylene), which had an O:C of 0.6-0.8 (Zhou et al. 2009). Since Massoli et al. (2010) showed that hygroscopicity increases with O:C, it is likely that our SOA coatings have an O:C < 0.6. We note that an O:C of 1.08 was measured for the toluene SOA used by Song et al. in their investigation of viscosity, produced in an oxidation flow reactor (Song et al. 2016). This discrepancy in O:C may explain the surprising lack of a residence time dependence in the 20% RH experiment,

discussed above; if SOA is less oxygenated, perhaps it is less viscous at 20% RH, allowing the soot-coating interface to reach equilibrium at both flow rates.

In summary, we have investigated the RH-dependence of soot aggregate restructuring induced by SOA coatings, and we have demonstrated that water has significant effects on the coating viscosity and surface tension, in addition to mass (or volume). At RH < 12%, SOA is too

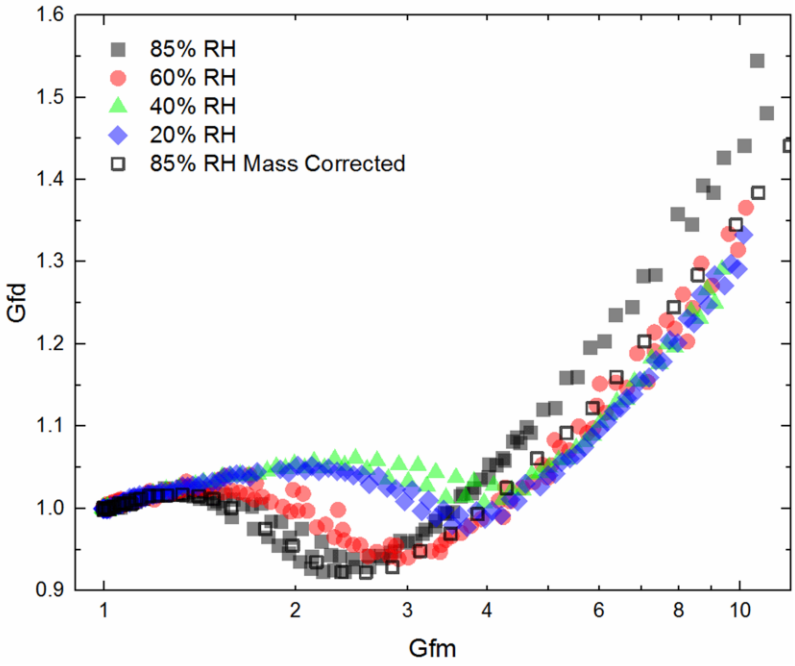

Figure 3.6. RH-dependent trends in diameter growth factor with increasing mass growth factor; for the 85% RH experiment, the trend in diameter growth factor with increasing water-corrected mass growth factor is also shown.

viscous to induce soot aggregate restructuring, and the coated aggregates become spherical only as the coating fills the voids of the unchanged aggregates. At RH ≥ 20%, water uptake decreases the viscosity of SOA sufficiently to induce soot aggregate restructuring, and the coated aggregates become spherical through a combination of collapse of the aggregates and accumulation of the coating. Since ambient RH is typically greater than 20% (Song et al. 2016), SOA-induced restructuring is an important mechanism in the morphological and optical evolution of soot aggregates. Furthermore, at RHs of 60 and 85%, water uptake significantly

increases the surface tension of the SOA coating, leading to incrementally greater soot aggregate restructuring, which may occur in very humid regions with soot sources - for example, coastal cities with active commercial harbors (Healy et al. 2009; Zhou et al. 2009; Evans et al. 2015). Future studies should investigate the effects of water on SOA coatings derived from other precursors and characterized by a range of O:C. For example, at a given RH, SOA from isoprene is less viscous than that from toluene (Song et al. 2016; Song et al. 2015), so it may cause restructuring at all ambient RHs. If so, water would affect restructuring only by increasing the coating mass (Khalizov et al. 2013) and surface tension. Our results provide crucial insights into the interactions between soot, SOA, and water that partly govern the complex climate effects of soot aggregates.

Chapter 4.

Conclusions

The relationships between soot aggregate restructuring induced by SOA and primary particle number and the effect of water on SOA coatings have been investigated. While the work here does not explain the complex interaction of soot aggregates with the environment in its entirety, it does provide key insights of smaller interactions to contribute to the whole. This section provides a summary of the research covered in this report, results, and possible topics for future work.

4.1 **Soot restructuring and primary particle number**

The evolution from initial to final morphologies of soot aggregates due to SOA coating was investigated by mobility and mass measurements, where soot was generated from three sources. For all aggregates, the evolution from the initial to final morphologies occurs in three distinct stages; however the coating mass to initiate each stage varied between initial mobility diameter and aggregate generating source. At a comparable initial mobility diameter, the aggregates from the diesel generator are less dense and had smaller constituent primary particle sizes than the aggregates from the two burners and restructure to a smaller final mobility diameter. Furthermore, for a given initial mobility diameter the extent of restructuring varies significantly with the soot generating source. For example, initially 100 nm aggregates from a diesel generator had an appreciable decrease in mobility diameter (Gfd = 0.92), but was not the case for the two burners (Gfd = 0.99). However, the ratio of final to initial aggregate mobility exhibits a linear relationship to the number of primary particles per aggregate regardless of source, indicating that the role the source of soot plays is dictating the size and number of primary particles in aggregates. The significance of the linear relationship observed is that

modelers can predict the extent of aggregate restructuring knowing only the number of primary particles per aggregate, which can be derived for soot with established mass-mobility relationships (Ghazi et al. 2013; Dastanpour et al. 2016b).

A topic of follow-up work may be to determine the relationship of final aggregate mobility diameters to the surface tension of SOA coatings. Although the current relationship reported is accurate for the representative anthropogenic SOA coating, it may only be applicable to coatings of similar surface tension. Since further restructuring can occur with coatings of higher surface tension; for example, aggregates generated from the premixed burner restructured to a mass-mobility exponent of three when coated with glycerol (Schnitzler et al. 2017).

4.2 **Humidity dependence of SOA**

The evolution from initial to final morphologies of soot aggregates due to SOA coating at controlled RHs of < 12, 20, 40, 60, or 85% was investigated by mobility and mass measurements. For RH < 12%, mobility increased uniformly with coating mass, indicating the coating was too viscous to induce appreciable aggregate restructuring. At RH ≥ 20%, the three stages of aggregate restructuring were observed. Furthermore, restructuring of aggregates was observed while the coating was still present on the aggregate, without the evaporation of the SOA coating. The coating mass required to initiate the stages of restructuring varied between controlled RHs, indicating a dependence of aggregate evolution on RH. For RH ≥ 60%, the extent of restructuring was larger than the restructuring observed for RHs 20 and 40%, which suggests that water affects the viscosity and surface tension of the coating. The observed aggregate restructuring at RH ≥ 20% is significant because ambient RH is generally greater than 20% (Song et al. 2016), suggesting that morphological and optical evolution of soot aggregates occur naturally in the environment. Furthermore, SOA coatings using a wide assortment of

precurosrs should be investigated, since SOA coatings derived different precursors have varying viscosities. Therefore it may be possible for aggregate restructuring to occur at all atmospherically relevant RHs given an SOA coating with sufficiently low viscosity.

4.3. **Conclusion**

This work here demonstrates that there is a relationship between the extent of aggregate restructuring due to SOA coatings with respect to soot aggregate properties and that water has a significant role in the properties SOA coating. The results from this work could be used in future theoretical aggregate restructuring studies to predict the resulting morphology of soot aggregates that are influenced by a known coating. Furthermore, the predicted end morphology of soot aggregates can be used in theoretical optical studies that investigate the changes in optical properties of soot aggregates. These can be included in atmospheric models by providing insight on the changes in soot aggregate morphology in the atmosphere due to photo-chemical aging, reducing the uncertainty in radiative forcing contributed by soot aggregates.

Bibliography

Atkinson, R. 2009. “Product Studies of Gas-Phase Reactions of Organic Compounds.” *Pure and Applied Chemistry* 70 (7): 1335–1343. doi:10.1351/pac199870071335.

Bambha, Ray P., Mark A. Dansson, Paul E. Schrader, and Hope A. Michelsen. 2013. “Effects of Volatile Coatings and Coating Removal Mechanisms on the Morphology of Graphitic Soot.” *Carbon* 61 (September): 80–96. doi:10.1016/j.carbon.2013.04.070.

Barone, Teresa L., John M.E. Storey, Adam D. Youngquist, and James P. Szybist. 2012. “An Analysis of Direct-Injection Spark-Ignition (DISI) Soot Morphology.” *Atmospheric Environment* 49 (March): 268–74. doi:10.1016/j.atmosenv.2011.11.047.

Bohren, C.F. 1983. *Absorption and Scattering of Light by Small Particles*. Absorption and Scattering of Light by Small Particles.

Bond, T. C., S. J. Doherty, D. W. Fahey, P. M. Forster, T. Berntsen, B. J. DeAngelo, M. G. Flanner, et al. 2013. “Bounding the Role of Black Carbon in the Climate System: A Scientific Assessment: BLACK CARBON IN THE CLIMATE SYSTEM.” *Journal of Geophysical Research: Atmospheres* 118 (11): 5380–5552. doi:10.1002/jgrd.50171.

Bond, Tami C., and Robert W. Bergstrom. 2006. “Light Absorption by Carbonaceous Particles: An Investigative Review.” *Aerosol Science and Technology* 40 (1): 27–67. doi:10.1080/02786820500421521.

Cappa, Christopher D., Timothy B. Onasch, Paola Massoli, Douglas R. Worsnop, Timothy S. Bates, Eben S. Cross, Paul Davidovits, et al. 2012. “Radiative Absorption Enhancements Due to the Mixing State of Atmospheric Black Carbon.” *Science* 337 (6098): 1078–81. doi:10.1126/science.1223447.

Dastanpour Ramin, Jocelyne M. Boone, and Steven N. Rogak. 2016a. “Automated Primary Particle Sizing of Nanoparticle Aggregates by TEM Image Analysis.” *Powder Technology* 295 (July): 218–24. doi:10.1016/j.powtec.2016.03.027.

Dastanpour Ramin, and Steven N. Rogak. 2016. “The Effect of Primary Particle Polydispersity on the Morphology and Mobility Diameter of the Fractal Agglomerates in Different Flow Regimes.” *Journal of Aerosol Science* 94 (April): 22–32. doi:10.1016/j.jaerosci.2015.12.005.

Dastanpour Ramin, Steven N. Rogak, Brian Graves, Jason Olfert, Maximilian L. Eggersdorfer, and Adam M. Boies. 2016b. “Improved Sizing of Soot Primary Particles Using Mass-Mobility Measurements.” *Aerosol Science and Technology* 50 (2): 101–9. doi:10.1080/02786826.2015.1130796.

Dastanpour Ramin, J. M. Boone, and S. N. Rogak. 2016c. *PCM Program*. http://www.aerosol.mech.ubc.ca/research/soot-and-nanoparticles.

DeCarlo, Peter F., Jay G. Slowik, Douglas R. Worsnop, Paul Davidovits, and Jose L. Jimenez. 2004. “Particle Morphology and Density Characterization by Combined Mobility and Aerodynamic Diameter Measurements. Part 2: Application to Combustion-Generated Soot Aerosols as a Function of Fuel Equivalence Ratio.” *Aerosol Science and Technology* 38 (12): 1206–22. doi:10.1080/027868290903916.

Dickau, Matthew, Jason Olfert, Marc E. J. Stettler, Adam Boies, Ali Momenimovahed, Kevin Thomson, Greg Smallwood, and Mark Johnson. 2016. “Methodology for Quantifying the Volatile Mixing State of an Aerosol.” *Aerosol Science and Technology* 50 (8): 759–72. doi:10.1080/02786826.2016.1185509.

Donahue, N. M., A. L. Robinson, C. O. Stanier, and S. N. Pandis. 2006. "Coupled Partitioning, Dilution, and Chemical Aging of Semivolatile Organics." *Environmental Science & Technology* 40 (8): 2635–43. doi:10.1021/es052297c.

Eggersdorfer, M.L., A.J. Gröhn, C.M. Sorensen, P.H. McMurry, and S.E. Pratsinis. 2012. "Mass-Mobility Characterization of Flame-Made ZrO2 Aerosols: Primary Particle Diameter and Extent of Aggregation." *Journal of Colloid and Interface Science* 387 (1): 12–23. doi:10.1016/j.jcis.2012.07.078.

Evans, M., N. Kholod, V. Malyshev, S. Tretyakova, E. Gusev, S. Yu, and A. Barinov. 2015. "Black Carbon Emissions from Russian Diesel Sources: Case Study of Murmansk." *Atmos. Chem. Phys.* 15 (14): 8349–59. doi:10.5194/acp-15-8349-2015.

Forstner, Hali J. L., Richard C. Flagan, and John H. Seinfeld. 1997. "Secondary Organic Aerosol from the Photooxidation of Aromatic Hydrocarbons: Molecular Composition." *Environmental Science & Technology* 31 (5): 1345–58. doi:10.1021/es9605376.

Ghazi, R., and J. S. Olfert. 2013. "Coating Mass Dependence of Soot Aggregate Restructuring due to Coatings of Oleic Acid and Dioctyl Sebacate." *Aerosol Science and Technology* 47 (2): 192–200. doi:10.1080/02786826.2012.741273.

Ghazi, Rouzbeh, Hugo Tjong, Arka Soewono, Steven N. Rogak, and Jason S. Olfert. 2013. "Mass, Mobility, Volatility, and Morphology of Soot Particles Generated by a McKenna and Inverted Burner." *Aerosol Science and Technology* 47 (4): 395–405. doi:10.1080/02786826.2012.755259.

Goldstein, Allen H., and Ian E. Galbally. 2007. "Known and Unexplored Organic Constituents in the Earth's Atmosphere." *Environmental Science & Technology* 41 (5): 1514–21. doi:10.1021/es072476p.

Guo, Song, Min Hu, Yun Lin, Mario Gomez-Hernandez, Misti L. Zamora, Jianfei Peng, Donald R. Collins, and Renyi Zhang. 2016. “OH-Initiated Oxidation of *M* -Xylene on Black Carbon Aging.” *Environmental Science & Technology* 50 (16): 8605–12. doi:10.1021/acs.est.6b01272.

Gysel, M., M. Laborde, A. A. Mensah, J. C. Corbin, A. Keller, J. Kim, A. Petzold, and B. Sierau. 2012. “Technical Note: The Single Particle Soot Photometer Fails to Reliably Detect PALAS Soot Nanoparticles.” *Atmospheric Measurement Techniques* 5 (12): 3099–3107. doi:10.5194/amt-5-3099-2012.

Hallquist, M., J. C. Wenger, U. Baltensperger, Y. Rudich, D. Simpson, M. Claeys, J. Dommen, et al. 2009. “The Formation, Properties and Impact of Secondary Organic Aerosol: Current and Emerging Issues.” *Atmos. Chem. Phys.* 9 (14): 5155–5236. doi:10.5194/acp-9-5155-2009.

Healy, Robert M., Ian P. O’Connor, Stig Hellebust, Arnaud Allanic, John R. Sodeau, and John C. Wenger. 2009. “Characterisation of Single Particles from in-Port Ship Emissions.” *Atmospheric Environment* 43 (40): 6408–14. doi:10.1016/j.atmosenv.2009.07.039.

Huff Hartz, Kara E., Joshua E. Tischuk, Man Nin Chan, Chak K. Chan, Neil M. Donahue, and Spyros N. Pandis. 2006. “Cloud Condensation Nuclei Activation of Limited Solubility Organic Aerosol.” *Atmospheric Environment* 40 (4): 605–17. doi:10.1016/j.atmosenv.2005.09.076.

Kahnert, M., and A. Devasthale. 2011. “Black Carbon Fractal Morphology and Short-Wave Radiative Impact: A Modelling Study.” *Atmospheric Chemistry & Physics* 11 (22): 11745–59. doi:10.5194/acp-11-11745-2011.

Kesselmeier, J., and M. Staudt. 1999. “Biogenic Volatile Organic Compounds (VOC): An Overview on Emission, Physiology and Ecology.” *Journal of Atmospheric Chemistry* 33 (1): 23–88. doi:10.1023/A:1006127516791.

Keywood, Melita, Maria Kanakidou, Andreas Stohl, Frank Dentener, Giacomo Grassi, C. P. Meyer, Kjetil Torseth, et al. 2013. “Fire in the Air: Biomass Burning Impacts in a Changing Climate.” *Critical Reviews in Environmental Science and Technology* 43 (1): 40–83. doi:10.1080/10643389.2011.604248.

Khalizov, Alexei F., Yun Lin, Chong Qiu, Song Guo, Don Collins, and Renyi Zhang. 2013. “Role of OH-Initiated Oxidation of Isoprene in Aging of Combustion Soot.” *Environmental Science & Technology* 47 (5): 2254–63. doi:10.1021/es3045339.

Khalizov, Alexei F., Huaxin Xue, Lin Wang, Jun Zheng, and Renyi Zhang. 2009. “Enhanced Light Absorption and Scattering by Carbon Soot Aerosol Internally Mixed with Sulfuric Acid.” *The Journal of Physical Chemistry A* 113 (6): 1066–74. doi:10.1021/jp807531n.

Kholghy, Mohammadreza, Meghdad Saffaripour, Christopher Yip, and Murray John Thomson. 2013. “The Evolution of Soot Morphology in a Laminar Coflow Diffusion Flame of a Surrogate for Jet A-1.” *Combustion and Flame* 160 (10): 2119–30. doi:10.1016/j.combustflame.2013.04.008.

Kralchevsky, P. A., V. N. Paunov, and Kuniaki Nagayama. 1995. “Lateral Capillary Interaction between Particles Protruding from a Spherical Liquid Layer.” *Journal of Fluid Mechanics* 299 (1): 105. doi:10.1017/S0022112095003442.

Kralchevsky, Peter A., and Kuniaki Nagayama. 2000. “Capillary Interactions between Particles Bound to Interfaces, Liquid Films and Biomembranes.” *Advances in Colloid and Interface Science* 85 (2): 145–192.

Kreidenweis, S M, M D Petters, and P J DeMott. 2008. “Single-Parameter Estimates of Aerosol Water Content.” *Environmental Research Letters* 3 (3): 035002. doi:10.1088/1748-9326/3/3/035002.

Lee, Jae Young, and Lynn M. Hildemann. 2014. “Surface Tensions of Solutions Containing Dicarboxylic Acid Mixtures.” *Atmospheric Environment* 89 (June): 260–67. doi:10.1016/j.atmosenv.2014.02.049.

Lian, Guoping, Colin Thornton, and Michael J. Adams. 1993. “A Theoretical Study of the Liquid Bridge Forces between Two Rigid Spherical Bodies.” *Journal of Colloid and Interface Science* 161 (1): 138–47. doi:10.1006/jcis.1993.1452.

Liu, Fengshan, Jérôme Yon, and Alexandre Bescond. 2016. “On the Radiative Properties of Soot Aggregates – Part 2: Effects of Coating.” *Journal of Quantitative Spectroscopy and Radiative Transfer* 172 (March): 134–45. doi:10.1016/j.jqsrt.2015.08.005.

Liu, Li, Michael I. Mishchenko, and W. Patrick Arnott. 2008. “A Study of Radiative Properties of Fractal Soot Aggregates Using the Superposition T-Matrix Method.” *Journal of Quantitative Spectroscopy and Radiative Transfer* 109 (15): 2656–63. doi:10.1016/j.jqsrt.2008.05.001.

Liu, Pengfei, Yue Zhang, and Scot T. Martin. 2013. “Complex Refractive Indices of Thin Films of Secondary Organic Materials by Spectroscopic Ellipsometry from 220 to 1200 Nm.” *Environmental Science & Technology* 47 (23): 13594–601. doi:10.1021/es403411e.

Ma, Xiaofei, Christopher D. Zangmeister, Julien Gigault, George W. Mulholland, and Michael R. Zachariah. 2013. “Soot Aggregate Restructuring during Water Processing.” *Journal of Aerosol Science* 66 (December): 209–19. doi:10.1016/j.jaerosci.2013.08.001.

Maricq, M.Matti, and Ning Xu. 2004. “The Effective Density and Fractal Dimension of Soot Particles from Premixed Flames and Motor Vehicle Exhaust.” *Journal of Aerosol Science* 35 (10): 1251–74. doi:10.1016/j.jaerosci.2004.05.002.

Massoli, P., A. T. Lambe, A. T. Ahern, L. R. Williams, M. Ehn, J. Mikkilä, M. R. Canagaratna, et al. 2010. “Relationship between Aerosol Oxidation Level and Hygroscopic Properties of Laboratory Generated Secondary Organic Aerosol (SOA) Particles.” *Geophysical Research Letters* 37 (24): L24801. doi:10.1029/2010GL045258.

Meakin, Paul, Bertram Donn, and George W. Mulholland. 1989. “Collisions between Point Masses and Fractal Aggregates.” *Langmuir* 5 (2): 510–18. doi:10.1021/la00086a038.

Mentel, Th F., J. Wildt, A. Kiendler-Scharr, E. Kleist, R. Tillmann, M. Dal Maso, R. Fisseha, et al. 2009. “Photochemical Production of Aerosols from Real Plant Emissions.” *Atmospheric Chemistry and Physics* 9 (13): 4387–4406.

Mikhailov, E. F., and S. S. Vlasenko. 2007. “Structure and Optical Properties of Soot Aerosol in a Moist Atmosphere: 1. Structural Changes of Soot Particles in the Process of Condensation.” *Izvestiya, Atmospheric and Oceanic Physics* 43 (2): 181–94. doi:10.1134/S0001433807020053.

Miljevic, Branka, Nicholas C. Surawski, Thor Bostrom, and Zoran D. Ristovski. 2012. “Restructuring of Carbonaceous Particles upon Exposure to Organic and Water Vapours.” *Journal of Aerosol Science* 47 (May): 48–57. doi:10.1016/j.jaerosci.2011.12.005.

Nakao, Shunsuke, Ping Tang, Xiaochen Tang, Christopher H. Clark, Li Qi, Eric Seo, Akua Asa-Awuku, and David Cocker. 2013. “Density and Elemental Ratios of Secondary Organic

Aerosol: Application of a Density Prediction Method." *Atmospheric Environment* 68 (April): 273–77. doi:10.1016/j.atmosenv.2012.11.006.

Odum, Jay R., Thorsten Hoffmann, Frank Bowman, Don Collins, Richard C. Flagan, and John H. Seinfeld. 1996. "Gas/Particle Partitioning and Secondary Organic Aerosol Yields." *Environmental Science & Technology* 30 (8): 2580–85. doi:10.1021/es950943+.

Olfert, J. S., and N. Collings. 2005. "New Method for Particle Mass Classification—the Couette Centrifugal Particle Mass Analyzer." *Journal of Aerosol Science* 36 (11): 1338–52. doi:10.1016/j.jaerosci.2005.03.006.

Olfert, J.S., J.P.R. Symonds, and N. Collings. 2007. "The Effective Density and Fractal Dimension of Particles Emitted from a Light-Duty Diesel Vehicle with a Diesel Oxidation Catalyst." *Journal of Aerosol Science* 38 (1): 69–82. doi:10.1016/j.jaerosci.2006.10.002.

Pagels, Joakim, Alexei F. Khalizov, Peter H. McMurry, and Renyi Y. Zhang. 2009. "Processing of Soot by Controlled Sulphuric Acid and Water Condensation—Mass and Mobility Relationship." *Aerosol Science and Technology* 43 (7): 629–40. doi:10.1080/02786820902810685.

Pankow, James F. 1994. "An Absorption Model of the Gas/Aerosol Partitioning Involved in the Formation of Secondary Organic Aerosol." *Atmospheric Environment* 28 (2): 189–193.

Park, Kihong, Feng Cao, David B. Kittelson, and Peter H. McMurry. 2003. "Relationship between Particle Mass and Mobility for Diesel Exhaust Particles." *Environmental Science & Technology* 37 (3): 577–83. doi:10.1021/es025960v.

Park, Kihong, David B. Kittelson, Michael R. Zachariah, and Peter H. McMurry. 2004. "Measurement of Inherent Material Density of Nanoparticle Agglomerates." *Journal of Nanoparticle Research* 6 (2): 267–272.

Parsons, Matthew T., Ihor Sydoryk, Alan Lim, Thomas J. McIntyre, John Tulip, Wolfgang Jäger, and Karen McDonald. 2011. "Real-Time Monitoring of Benzene, Toluene, and P-Xylene in a Photoreaction Chamber with a Tunable Mid-Infrared Laser and Ultraviolet Differential Optical Absorption Spectroscopy." *Applied Optics* 50 (4): A90–A99.

Peng, Jianfei, Min Hu, Song Guo, Zhuofei Du, Jing Zheng, Dongjie Shang, Misti Levy Zamora, et al. 2016. "Markedly Enhanced Absorption and Direct Radiative Forcing of Black Carbon under Polluted Urban Environments." *Proceedings of the National Academy of Sciences* 113 (16): 4266–71. doi:10.1073/pnas.1602310113.

Penner, Joyce E. 1999. *Aviation and the Global Atmosphere: A Special Report of the Intergovernmental Panel on Climate Change*. Cambridge University Press.

Petters, M. D., and S. M. Kreidenweis. 2007. "A Single Parameter Representation of Hygroscopic Growth and Cloud Condensation Nucleus Activity." *Atmos. Chem. Phys.* 7 (8): 1961–71. doi:10.5194/acp-7-1961-2007.

Piccot, Stephen D., Joel J. Watson, and Julian W. Jones. 1992. "A Global Inventory of Volatile Organic Compound Emissions from Anthropogenic Sources." *Journal of Geophysical Research: Atmospheres* 97 (D9): 9897–9912. doi:10.1029/92JD00682.

Qiu, Chong, Alexei F. Khalizov, and Renyi Zhang. 2012. "Soot Aging from OH-Initiated Oxidation of Toluene." *Environmental Science & Technology* 46 (17): 9464–72. doi:10.1021/es301883y.

Radney, James G., Rian You, Xiaofei Ma, Joseph M. Conny, Michael R. Zachariah, Joseph T. Hodges, and Christopher D. Zangmeister. 2014. “Dependence of Soot Optical Properties on Particle Morphology: Measurements and Model Comparisons.” *Environmental Science & Technology* 48 (6): 3169–76. doi:10.1021/es4041804.

Radney, James G., and Christopher D. Zangmeister. 2016. “Practical Limitations of Aerosol Separation by a Tandem Differential Mobility Analyzer–aerosol Particle Mass Analyzer.” *Aerosol Science and Technology* 50 (2): 160–72. doi:10.1080/02786826.2015.1136733.

Ramanathan, V., and G. Carmichael. 2008. “Global and Regional Climate Changes due to Black Carbon.” *Nature Geoscience* 1 (4): 221–27. doi:10.1038/ngeo156.

Rogak, Steven N., Richard C. Flagan, and Hung V. Nguyen. 1993. “The Mobility and Structure of Aerosol Agglomerates.” *Aerosol Science and Technology* 18 (1): 25–47. doi:10.1080/02786829308959582.

Ruiz, Pablo A., Joy E. Lawrence, Stephen T. Ferguson, Jack M. Wolfson, and Petros Koutrakis. 2006. “A Counter-Current Parallel-Plate Membrane Denuder for the Non-Specific Removal of Trace Gases.” *Environmental Science & Technology* 40 (16): 5058–63. doi:10.1021/es060563w.

Saathoff, H., K.-H. Naumann, M. Schnaiter, W. Schöck, O. Möhler, U. Schurath, E. Weingartner, M. Gysel, and U. Baltensperger. 2003. “Coating of Soot and (NH4)2SO4 Particles by Ozonolysis Products of α-Pinene.” *Journal of Aerosol Science* 34 (10): 1297–1321. doi:10.1016/S0021-8502(03)00364-1.

Schnaiter, M. 2005. “Absorption Amplification of Black Carbon Internally Mixed with Secondary Organic Aerosol.” *Journal of Geophysical Research* 110 (D19). doi:10.1029/2005JD006046.

Schnitzler, Elijah G., Ashneil Dutt, André M. Charbonneau, Jason S. Olfert, and Wolfgang Jäger. 2014. “Soot Aggregate Restructuring Due to Coatings of Secondary Organic Aerosol Derived from Aromatic Precursors.” *Environmental Science & Technology* 48 (24): 14309–16. doi:10.1021/es503699b.

Schnitzler, Elijah G., Jakub M. Gac, and Wolfgang Jäger. 2017. “Coating Surface Tension Dependence of Soot Aggregate Restructuring.” *Journal of Aerosol Science* 106 (April): 43–55. doi:10.1016/j.jaerosci.2017.01.005.

Schulz, M., C. Textor, S. Kinne, Y. Balkanski, S. Bauer, T. Berntsen, T. Berglen, et al. 2006. “Radiative Forcing by Aerosols as Derived from the AeroCom Present-Day and Pre-Industrial Simulations.” *Atmospheric Chemistry & Physics* 6 (12/2): 5225–46.

Schwarz, J. P., R. S. Gao, J. R. Spackman, L. A. Watts, D. S. Thomson, D. W. Fahey, T. B. Ryerson, et al. 2008. “Measurement of the Mixing State, Mass, and Optical Size of Individual Black Carbon Particles in Urban and Biomass Burning Emissions.” *Geophysical Research Letters* 35 (13): L13810. doi:10.1029/2008GL033968.

Shao, Ping, Junlin An, Jinyuan Xin, Fangkun Wu, Junxiu Wang, Dongsheng Ji, and Yuesi Wang. 2016. “Source Apportionment of VOCs and the Contribution to Photochemical Ozone Formation during Summer in the Typical Industrial Area in the Yangtze River Delta, China.” *Atmospheric Research* 176–177 (July): 64–74. doi:10.1016/j.atmosres.2016.02.015.

Simpson, I. J., N. J. Blake, B. Barletta, G. S. Diskin, H. E. Fuelberg, K. Gorham, L. G. Huey, et al. 2010. “Characterization of Trace Gases Measured over Alberta Oil Sands Mining Operations: 76 Speciated C2–C10 Volatile Organic Compounds (VOCs), CO2, CH4, CO,

NO, NO2, NOy, O3 and SO2." *Atmos. Chem. Phys.* 10 (23): 11931–54. doi:10.5194/acp-10-11931-2010.

Song, M., P. F. Liu, S. J. Hanna, Y. J. Li, S. T. Martin, and A. K. Bertram. 2015. "Relative Humidity-Dependent Viscosities of Isoprene-Derived Secondary Organic Material and Atmospheric Implications for Isoprene-Dominant Forests." *Atmospheric Chemistry and Physics* 15 (9): 5145–59. doi:10.5194/acp-15-5145-2015.

Song, Mijung, Pengfei F. Liu, Sarah J. Hanna, Rahul A. Zaveri, Katie Potter, Yuan You, Scot T. Martin, and Allan K. Bertram. 2016. "Relative Humidity-Dependent Viscosity of Secondary Organic Material from Toluene Photo-Oxidation and Possible Implications for Organic Particulate Matter over Megacities." *Atmospheric Chemistry and Physics* 16 (14): 8817–30. doi:10.5194/acp-16-8817-2016.

Sorensen, C. M. 2011. "The Mobility of Fractal Aggregates: A Review." *Aerosol Science and Technology* 45 (7): 765–79. doi:10.1080/02786826.2011.560909.

Tritscher, Torsten, Zsófia Jurányi, Maria Martin, Roberto Chirico, Martin Gysel, Maarten F Heringa, Peter F DeCarlo, et al. 2011. "Changes of Hygroscopicity and Morphology during Ageing of Diesel Soot." *Environmental Research Letters* 6 (3): 034026. doi:10.1088/1748-9326/6/3/034026.

TSI, 2006, "Model 3776 Ultrafine Condensation Particle Counter, Operation and Service Manual" [PDF], Revision B.

TSI. 2009. "Series 3080 Electrostatic Classifiers, Operation and Service Manual" [PDF], Revision J. William C. Hinds. 1999. *Aerosol Technology: Properties, Behavior, and Measurement of Airborne Particles, 2nd Edition*.

Wu, Yu, Tianhai Cheng, Lijuan Zheng, and Hao Chen. 2017. “Sensitivity of Mixing States on Optical Properties of Fresh Secondary Organic Carbon Aerosols.” *Journal of Quantitative Spectroscopy and Radiative Transfer*, January. doi:10.1016/j.jqsrt.2017.01.013.

Xue, Huaxin, Alexei F. Khalizov, Lin Wang, Jun Zheng, and Renyi Zhang. 2009. “Effects of Coating of Dicarboxylic Acids on the Mass- Mobility Relationship of Soot Particles.” *Environmental Science & Technology* 43 (8): 2787–2792.

Zhao, D. F., A. Buchholz, B. Kortner, P. Schlag, F. Rubach, H. Fuchs, A. Kiendler-Scharr, et al. 2016. “Cloud Condensation Nuclei Activity, Droplet Growth Kinetics, and Hygroscopicity of Biogenic and Anthropogenic Secondary Organic Aerosol (SOA).” *Atmospheric Chemistry and Physics* 16 (2): 1105–21. doi:10.5194/acp-16-1105-2016.

Zhou, Xuehua, Jian Gao, Tao Wang, Waishing Wu, and Wenxing Wang. 2009. “Measurement of Black Carbon Aerosols near Two Chinese Megacities and the Implications for Improving Emission Inventories.” *Atmospheric Environment* 43 (25): 3918–24. doi:10.1016/j.atmosenv.2009.04.062.